Monthly Notices
of the
ROYAL ASTRONOMICAL SOCIETY

MNRAS **436,** 430–448 (2013)
Advance Access publication 2013 September 28

doi:10.1093/mnras/stt1577

The SCUBA-2 Cosmology Legacy Survey: demographics of the 450-μm population

I. G. Roseboom,[1]★ J. S. Dunlop,[1] M. Cirasuolo,[1] J. E. Geach,[2] I. Smail,[3] M. Halpern,[4] P. van der Werf,[5] O. Almaini,[6] V. Arumugam,[7] V. Asboth,[4] R. Auld,[8] A. Blain,[9] M. N. Bremer,[10] J. Bock,[11,12] R. A. A. Bowler,[1] F. Buitrago,[1] E. Chapin,[4,13] S. Chapman,[14] A. Chrysostomou,[15,16] C. Clarke,[17] A. Conley,[18] K. E. K. Coppin,[2] A. L. R. Danielson,[3] D. Farrah,[19] J. Glenn,[18] E. Hatziminaoglou,[20] E. Ibar,[7] R. J. Ivison,[1,7] T. Jenness,[16,21] E. van Kampen,[20] A. Karim,[3] T. Mackenzie,[4] G. Marsden,[4] R. Meijerink,[22] M. J. Michałowski,[1,23]† S. J. Oliver,[17] M. J. Page,[24] E. Pearson,[8] Douglas Scott,[4] J. M. Simpson,[3] D. J. B. Smith,[15] M. Spaans,[22] A. M. Swinbank,[3] M. Symeonidis,[24] T. Targett,[1] E. Valiante,[8] M. Viero,[11] L. Wang,[3] C. J. Willott[25] and M. Zemcov[11,12]

[1]*Institute for Astronomy, University of Edinburgh, Royal Observatory, Blackford Hill, Edinburgh EH9 3HJ, UK*
[2]*Department of Physics, Ernest Rutherford Building, McGill University, 3600 rue University, Montréal, QC, H3A 2T8, Canada*
[3]*Institute for Computational Cosmology, Department of Physics, Durham University, South Road, Durham DH1 3LE, UK*
[4]*Department of Physics & Astronomy, University of British Columbia, 6224 Agricultural Road, Vancouver, BC V6T 1Z1, Canada*
[5]*Leiden Observatory, Leiden University, PO Box 9513, NL-2300 RA Leiden, the Netherlands*
[6]*School of Physics and Astronomy, University of Nottingham, University Park, Nottingham NG9 2RD, UK*
[7]*UK Astronomy Technology Centre, Royal Observatory, Blackford Hill, Edinburgh EH9 3HJ, UK*
[8]*Cardiff School of Physics and Astronomy, Cardiff University, Queens Buildings, The Parade, Cardiff CF24 3AA, UK*
[9]*Department of Physics & Astronomy, University of Leicester, University Road, Leicester LE1 7RH, UK*
[10]*H. H. Wills Physics Laboratory, University of Bristol, Tyndall Avenue, Bristol BS8 1TL, UK*
[11]*California Institute of Technology, 1200 E. California Blvd., Pasadena, CA 91125, USA*
[12]*Jet Propulsion Laboratory, 4800 Oak Grove Drive, Pasadena, CA 91109, USA*
[13]*XMM SOC, ESAC, Apartado 78, E-28691 Villanueva de la Canada, Madrid, Spain*
[14]*Department of Physics and Atmospheric Science, Dalhousie University Halifax, NS B3H 3J5, Canada*
[15]*Centre for Astrophysics Research, University of Hertfordshire, College Lane, Hatfield, Hertfordshire AL10 9AB, UK*
[16]*Joint Astronomy Centre, 660 N. Aóhoku Place, University Park, Hilo, Hawaii 96720, USA*
[17]*Astronomy Centre, Department of Physics & Astronomy, University of Sussex, Brighton BN1 9QH, UK*
[18]*Department of Astrophysical and Planetary Sciences, CASA 389-UCB, University of Colorado, Boulder, CO 80309, USA*
[19]*Department of Physics, Virginia Polytechnic Institute & State University, 910 Drillfield Drive, Blacksburg, VA 24061, USA*
[20]*ESO, Karl-Schwarzschild-Str. 2, D-85748 Garching bei München, Germany*
[21]*Astronomy Department, Cornell University, Ithaca, NY 14853, USA*
[22]*Kapteyn Astronomical Institute, University of Groningen, PO Box 800, NL-9700 AV Groningen, the Netherlands*
[23]*Sterrenkundig Observatorium, Universiteit Gent, Krijgslaan 281 S9, B-9000 Gent, Belgium*
[24]*Mullard Space Science Laboratory, University College London, Holmbury St Mary Dorking, Surrey RH5 6NT, UK*
[25]*Herzberg Institute of Astrophysics, National Research Council, 5071 West Saanich Rd, Victoria, BC V9E 2E7, Canada*

Accepted 2013 August 20. Received 2013 August 9; in original form 2013 May 15

ABSTRACT

We investigate the multiwavelength properties of a sample of 450-μm-selected sources from the SCUBA-2 Cosmology Legacy Survey. A total of 69 sources were identified above 4σ in deep SCUBA-2 450-μm observations overlapping the UDS and COSMOS fields and covering 210 arcmin^2 to a typical depth of $\sigma_{450} = 1.5$ mJy. Reliable cross-identifications are found for

★E-mail: igr@roe.ac.uk
†FWO Pegasus Marie Curie Fellow.

58 sources (84 per cent) in *Spitzer* and *Hubble Space Telescope* WFC3/IR data. The photometric redshift distribution (dN/dz) of 450-μm-selected sources is presented, showing a broad peak in the redshift range $1 < z < 3$ and a median of $z = 1.4$. Combining the SCUBA-2 photometry with *Herschel* SPIRE data from HerMES, the submm spectral energy distribution (SED) is examined via the use of modified blackbody fits, yielding aggregate values for the IR luminosity, dust temperature and emissivity of $\langle L_{\rm IR}\rangle = 10^{12\pm0.8}\,{\rm L}_\odot$, $\langle T_{\rm D}\rangle = 42 \pm 11\,{\rm K}$ and $\langle \beta_{\rm D}\rangle = 1.6 \pm 0.5$, respectively. The relationship between these SED parameters and the physical properties of galaxies is investigated, revealing correlations between $T_{\rm D}$ and $L_{\rm IR}$ and between $\beta_{\rm D}$ and both stellar mass and effective radius. The connection between the star formation rate (SFR) and stellar mass is explored, with 24 per cent of 450-μm sources found to be 'starbursts', i.e. displaying anomalously high specific SFRs. However, both the number density and observed properties of these 'starburst' galaxies are found to be consistent with the population of normal star-forming galaxies.

Key words: galaxies: evolution – galaxies: starburst – submillimetre: galaxies.

1 INTRODUCTION

A key goal for observational studies of galaxy formation has been to build a complete picture of star formation over cosmic time. Much of the effort in the last two decades has been focused on tracers in two distinct wavelength ranges: the near-to-far-ultraviolet (UV) and the far-infrared/submm. These wavelengths are excellent tracers of star formation in distant galaxies; the UV continuum originates primarily from massive, short-lived stars, and the far-infrared (IR) from dust that envelops star-forming regions and re-processes this UV continuum.

Despite this close physical connection, these tracers have so far offered somewhat different views of the high-redshift ($z > 1$) Universe. Star-forming galaxies identified in the rest-frame UV are numerous, with moderate star formation rates (SFRs $\sim 10\,{\rm M}_\odot\,{\rm yr}^{-1}$; Madau et al. 1996; Reddy et al. 2006) while those detected in the submm (submm galaxies, SMGs) are rarer (by a factor of around 1/100 in surface density) and have extremely high SFRs (100–1000 $\rm M_\odot\,yr^{-1}$; Smail, Ivison & Blain 1997; Barger et al. 1998; Hughes et al. 1998; Chapman et al. 2005; Michałowski, Hjorth & Watson 2010). Traditionally, these disparate properties have been interpreted as a natural extension of the behaviour seen in the local Universe, where UV-bright galaxies are common and typically star-forming discs, while the most IR-luminous galaxies (ULIRGs; $L_{\rm IR} > 10^{12}\,{\rm L}_\odot$) are rare and mostly the result of major mergers (e.g. Sanders et al. 1988; Farrah et al. 2001).

In recent years, it has become clear that this single definition for SMGs cannot be completely accurate. While some SMGs are associated with merger events (e.g. Swinbank et al. 2010; Alaghband-Zadeh et al. 2012), it appears that a significant fraction of SMGs have disc-like morphologies (Targett et al. 2011, 2013). However, morphological studies of galaxies in the distant Universe require high resolution and sensitivity, restricting the size of samples studied in this way, and are difficult to interpret given the redshift (K-correction) and other selection effects.

Meanwhile, the role of SMGs in galaxy formation has been brought into focus by the emerging notion of a so-called 'main sequence' for star-forming galaxies. Large-scale studies of UV-selected samples have shown that, for a given redshift, the ratio of the SFR to the stellar mass [often referred to as the specific SFR (sSFR)] is roughly constant (Daddi et al. 2007; Elbaz et al. 2007; Noeske et al. 2007; Karim et al. 2011). This main sequence has been taken as strong evidence of in situ star formation (as opposed to mergers) being the dominant process in building stellar mass in galaxies at $z > 1$ (Rodighiero et al. 2011), as mergers are thought to greatly enhance the sSFR (e.g. Mihos & Hernquist 1994). The sSFR of SMGs has thus become of much interest, with variations in stellar mass estimates leading to opposing claims of SMGs lying off (Hainline et al. 2011) and on the main sequence (Michałowski et al. 2012).

Interestingly, simulations of galaxies at $z \sim 2$ suggest that this dichotomous behaviour is to be expected, as the typical sensitivity and beam size of submm surveys (e.g. SHADES, LESS; $\sigma_{850} \sim 1$ mJy; Mortier et al. 2005; Weiß et al. 2009) are such that they should be sensitive to both merger-induced starbursts and the massive end of the star-forming disc population (Hayward et al. 2012).

Thus, while SMGs may not form a single homogeneous population, submm surveys are able to trace the most highly star-forming galaxies at $z \sim 2$ in a way not currently possible at other wavelengths. With the advent of *Herschel*[1] (Pilbratt et al. 2010), large-scale ($\gtrsim$100 deg^2) multiband submm surveys have become possible for the first time (e.g. HerMES,[2] H-ATLAS; Eales et al. 2010; Oliver et al. 2012). The scientific yield from these surveys has been revolutionary in two ways. First, the massive increase in survey volume (from increases in both depth and area) over existing submm data sets has produced a significant leap in our knowledge of the aggregate properties of the submm population, e.g. their number density (Clements et al. 2010; Glenn et al. 2010; Oliver et al. 2010; Béthermin et al. 2011, 2012a) and clustering properties (Cooray et al. 2010; Maddox et al. 2010; Amblard et al. 2011; van Kampen et al. 2012; Viero et al. 2013). Secondly, the multiband nature of the *Herschel* data, with six far-IR/submm bands covering the observed-frame 70- to 500-μm range, has meant that the physical information contained in the far-IR spectral energy distribution (SED) can be probed for the first time (e.g. Elbaz et al. 2010; Hwang et al. 2010; Magdis et al. 2010; Smith et al. 2012b; Symeonidis et al. 2013).

However, the interpretation of the *Herschel* data sets has been hampered by the large beam size of *Herschel* at submm wavelengths ($\gtrsim$20 arcsec). The resulting confusion noise ($\sim$6 mJy 1σ; Nguyen et al. 2010) for SPIRE imaging has meant that for the faintest SPIRE sources (i.e. <30 mJy) both accurate cross-identifications and flux densities require the use of ancillary data at IR or radio

[1] *Herschel* is an ESA space observatory with science instruments provided by European-led Principal Investigator consortia and with important participation from NASA.
[2] hermes.sussex.ac.uk

wavelengths (e.g. Roseboom et al. 2010, 2012a). This dependence on ancillary data has meant that the *Herschel* surveys have struggled to significantly increase the observable parameter space, in terms of $L_{\rm IR}-z$, for IR galaxies.

While Atacama Large Millimeter Array (ALMA) will eventually produce deep, high-resolution, blank field submm imaging, its limited field of view ($\ll$1 arcmin at 450 μm) means that even moderately wide-area surveys (e.g. $>$100 arcmin^2) would be very observationally expensive. For this reason, SCUBA-2 on the 15-m James Clerk Maxwell Telescope (JCMT) occupies a unique niche in submm imaging capability (Holland et al. 2013). With a mapping speed more than 100 times faster than the original SCUBA and a beam size of 8 arcsec at 450 μm, SCUBA-2 offers for the first time both the sensitivity and angular resolution required to perform sensitive studies of individual galaxies at $z > 1$ without concerns about source confusion.

The SCUBA-2 Cosmology Legacy Survey (S2CLS) is the largest programme that will be undertaken with SCUBA-2, aiming to map 0.6 ($\sim$10) deg^2 of the best extragalactic survey fields at 450 (850) μm to a depth of $\sigma \sim 1$ mJy. 12 months of S2CLS observing, equating to over 100 h on-sky, have now been obtained, with the first results on the deep number counts at 450 μm presented by Geach et al. (2013). Here, we investigate the multiwavelength properties of the galaxies selected at 450 μm using preliminary data in two deep S2CLS 450-μm fields: COSMOS and UDS.

In Section 2, we introduce the data sets utilized in this work and Section 3 describes the process undertaken to find multiwavelength identifications for the SCUBA-2 sources. In Section 4, we present our results: the identification statistics and demographics for our 450-μm sample (Section 4.1) and a comparison to measurements of the same sources with *Herschel* SPIRE (Section 4.2). The scientific implications of these results are investigated via a detailed look at submm SEDs (Sections 5.1 and 5.2), and an investigation into the stellar masses and sSFRs of 450-μm sources (Section 5.3). Finally, we present our conclusions in Section 6. Throughout we assume a Λ cold dark matter cosmology with $\Omega_\Lambda = 0.7$, $\Omega_{\rm m} = 0.3$ and $H_0 = 70$ km s^{-1} Mpc^{-1}. All SFR and stellar mass estimates presented assume, or have been converted to, a Chabrier (2003) initial mass function (IMF).

2 DATA

2.1 SCUBA-2

The starting point for this study is the 450- and 850-μm imaging taken as part of the S2CLS in the deep extragalactic COSMOS and UDS fields. Observations were taken with SCUBA-2 on the 15-m JCMT between 2011 October 2011 and 2012 July. For these deep fields, only the best observing conditions were used, i.e. $\tau_{225\,\rm GHz} < 0.05$. The standard 'daisy' mapping pattern (Holland et al. 2013) was used, with observations broken into 30 min scans. All data are reduced using the SMURF package[3] V1.4.0 (Chapin et al. 2013). The default 'blank field' configuration was used, although with the Fourier filtering increased to 1.3 Hz (equivalent to 120 arcsec at the SCUBA-2 scan rate). Flux calibration between pW and Jy is performed using the SCUBA-2 flux calibration factors appropriate for this version of SMURF: 606 Jy pW^{-1} beam^{-1} for 450 μm and 556 Jy pW^{-1} beam^{-1} for 850 μm (Dempsey et al. 2013).[4] Table 1 details the number of scans taken in each field and the corresponding depths. Noise-only maps of our SCUBA-2 images are produced from the data themselves, by inverting a random half of the individual scans before combining (Weiß et al. 2009; Austermann et al. 2010). These noise-only maps are used to estimate the completeness and reliability for our source detection algorithm.

Table 1. Details of deep S2CLS fields used in this paper.

Field	RA (°)	Dec. (°)	$N_{\rm scans}$	$\sigma_{450}{}^a$ (mJy)	$\sigma_{850}{}^a$ (mJy)	$N(>4\sigma)$
COSMOS	150.124	2.29	114	1.2	0.18	57
UDS	34.375	−5.2	29	2.3	0.32	12

[a]For a point source estimated from exposure time in the deepest region of the map, and not including any contribution from confusion.

Point sources are identified in the combined SCUBA-2 450-μm images by convolving the map with a 'matched filter' and looking for peaks which have a signal-to-noise ratio (SNR) of better than 4. The matched filter is constructed by first estimating the background on large scales by convolving the map with a Gaussian of full width at half-maximum (FWHM) = 30 arcsec. This background is then subtracted from the original map, and the background-subtracted image is convolved with the effective point source response function (PRF): a Gaussian of FWHM = 8 arcsec which has been 'background subtracted' in the same way (see discussion in section 4.2 of Chapin et al. 2013).

A total of 69 sources are identified across the two fields above an SNR of 4. The SNR threshold of 4 is used as this is found to produce a false positive detection rate of 5 per cent, which is considered acceptable for the purposes of this work. Only regions with good coverage (i.e. $\sigma_{450} < 5$ mJy) are used, limiting the area considered in COSMOS and UDS to the central 142 and 77 arcmin^2, respectively. Table 1 details the breakdown of these sources across the two fields and their typical noise properties, while Geach et al. (2013) present the number counts derived from the sources detected in the COSMOS field.

Photometry at 850 μm is performed simultaneously by assuming the detected 450-μm positions and the PRF at 850 μm, assumed to be a Gaussian with FWHM = 14.6 arcsec. The confusion noise at 850 μm for SCUBA-2 is predicted to be 0.3 mJy (Béthermin et al. 2011) and so our images will be confusion noise limited in the deepest regions. To account for this, we add this addition confusion noise to our instrumental noise estimates in quadrature. A full list of the 450-μm sources detected in the COSMOS and UDS fields is given in Tables A1 and A2, respectively. Analysis and catalogues of these deep 850-μm pointings independent of the 450-μm data will be present in future work.

The completeness of the 450-μm source catalogue is assessed by inserting sources of known flux into the noise-only maps. A total of 10^4 test sources are used, split into 10 logarithmically spaced flux bins between 1 and 60 mJy. In order to not adversely affect the overall map statistics, test sources are injected into, and recovered from, the noise-only maps in groups of 20 at a time, resulting in a total of 2000 simulated maps. Sources are recovered from each of these simulated maps using the same methods as the real maps. The completeness as a function of flux is assessed by taking the ratio of the total number of detected sources to the number injected into the noise-only maps.

[3] http://www.starlink.ac.uk/docs/sun258.htx/sun258.html

[4] http://www.jach.hawaii.edu/JCMT/continuum/scuba2/scuba2_relations.html

2.2 *Herschel* SPIRE

Overlapping *Herschel* SPIRE (Griffin et al. 2010) data exist for both of our S2CLS fields from the HerMES project (Oliver et al. 2012). While the instrumental noise of SPIRE data is similar to the SCUBA-2 data at 450 μm (i.e. $\sigma = 1$–2 mJy), the confusion noise is almost five times higher (∼6 mJy; Nguyen et al. 2010). Thus, to obtain reasonable SPIRE photometry for our 450-μm sources, we must resort to using the prior-based methods described in Roseboom et al. (2010) and Roseboom et al. (2012a, henceforth R12). Specifically, we follow the methodology presented in R12, with the minor difference that the 4.5-μm positions of 450-μm sources (as determined by our identification process in Section 3) are considered in conjunction with 24-μm sources. This work makes use of SPIRE images produced by HerMES, as described in Levenson et al. (2010), with updates in Viero et al. (2013). As in R12, weightings are used to ensure that rarer sources are upweighted in comparison to more common ones. As the surface density of 450-μm detected sources is about 10 times lower than that of 24-μm sources, the 450-μm sources typically have higher weightings and are hence given preference in highly degenerate situations (e.g. a 450- and a 24-μm source separated by less than one pixel in SPIRE imaging).

2.3 Other ancillary data and photometric redshifts

The deep S2CLS fields were chosen due to the large amount of ancillary data available at optical and near-IR wavelengths, in particular the ongoing *Hubble Space Telescope* (*HST*) Cosmic Assembly Near-infrared Deep Extragalactic Legacy Survey (CANDELS)[5] which is imaging 0.2 deg^2 to a depth of $F160W < 26.5$ mag (Grogin et al. 2011; Koekemoer et al. 2011). In both COSMOS and UDS, we produce new multiwavelength catalogues by first convolving all available optical/near-IR imaging to a common PSF (0.8 arcsec FWHM) and then performing aperture photometry using the CANDELS $F160W$ as the detection band (see Bowler et al. 2012 for details). For each source in these catalogues, we calculate photometric redshifts and stellar masses using the approach presented in Cirasuolo et al. (2010) and Michałowski et al. (2012), which we briefly summarize here. Optical near-IR photometry is compared to a representative grid of galaxy templates, generated from Bruzual & Charlot (2003) models. Small adjustments to the zero-points of the photometric bands are made by testing the photo-z algorithm against available spectroscopic redshifts in both fields (i.e. zCOSMOS, UDSz; Lilly et al. 2007; Almaini et al., in preparation). After adjusting the zero-points, and excluding sources with poor fits to the templates (i.e. those with a chi-squared statistic of $\chi^2 > 20$), the typical photo-z accuracy is found to be $\mathrm{d}z/(1+z) = 0.03$. Meanwhile, stellar masses are estimated assuming a two-component stellar population, an old population and a recent 'burst'. As discussed by Michałowski et al. (2012), the use of these two-component models to infer the mass of submm-luminous galaxies results in an ∼0.3 dex uncertainty in the mass estimates.

Spitzer IRAC 3.6- and 4.5-μm photometry is added by directly fitting the IRAC images using K-band positions and shape information (UKIDSS in UDS, UltraVISTA in COSMOS). The 5.8- and 8-μm IRAC channels are not considered as they suffer from source blending issues due to the large IRAC PSF at these wavelengths. Across most of the redshift range of interest, these channels do not probe the stellar light from galaxies, and hence their omission does not significantly affect photo-z and stellar mass estimates.

Spitzer MIPS 24-μm photometry in COSMOS is performed using the STARFINDER package (Diolaiti et al. 2000) on the public SCOSMOS image (Le Floćh et al. 2009), as described in Roseboom et al. (2012b).

3 IDENTIFICATIONS FOR SCUBA-2 SOURCES

Despite the relatively small beam of SCUBA-2 at 450 μm, the low-SNR nature of our source catalogues ($>4\sigma$), as well as the matching depth at optical/near-IR wavelengths required to find identifications ($K_{\mathrm{AB}} \sim 24$; Oliver et al. 2012), means that simple nearest-neighbour matching is not sufficient. Thus, we make use of the likelihood ratio (LR) formalism, as presented by Sutherland & Saunders (1992), to make statistically reliable cross-identifications between our SCUBA-2 450-μm source lists and the ancillary data.

In order to utilize both colour and mid-IR information in the matching process, we extend the LR method in a similar fashion as in Chapin et al. (2011, henceforth C11). Specifically, for each match between a 450-μm source i and an ancillary source j within a maximum separation r_{max}, we calculate

$$L_{i,j} = \frac{q(S,c)\mathrm{e}^{-r_{i,j}^2/2\sigma_i^2}}{2\pi\sigma_i^2\rho(S,c)}, \quad (1)$$

where $r_{i,j}$ is the separation between the two sources, σ_i is the positional uncertainty of the SCUBA-2 450-μm source, $\rho(S, c)$ is the probability of finding a background source with the flux density S and a colour c, while similarly $q(S, c)$ is the prior probability of a true match having this flux and IRAC colour. For this work, the matching flux density S is the 24-μm value where $S_{24} > 80$ μJy (4σ for the fields considered here), otherwise the 4.5-μm value is used. The 24-μm identifications are generally preferred as the areal density of 24-μm sources is significantly lower than 4.5-μm sources (∼10 times), and the 24-μm photometry is typically dominated by thermal dust emission as opposed to starlight which dominates at 4.5 μm. While both bands could have been used (as in C11), we find $S_{4.5}$ and S_{24} to be correlated (a Spearman rank test gives a correlation coefficient of 0.6), and hence there is little extra discriminatory power in using both bands. For the colour c, we use the colour between the two IRAC channels at 3.6 and 4.5 μm: $[3.6-4.5]$.

For the positional uncertainty, σ_i, we assume $\sigma_i = 0.6\,\mathrm{FWHM/SNR}$ (Ivison et al. 2007), with a minimum uncertainty of 1 arcsec to account for the overall pointing accuracy of JCMT.

The prior probabilities $q(S, c)$ and $\rho(S, c)$ are calculated directly from the data in a similar fashion to C11. For each source in our 450-μm catalogue, we find all of the potential matches in the IRAC and 24-μm catalogues within a maximum search radius of 4 arcsec. This radius was chosen as it is $\sim\frac{1}{2}$ FWHM, i.e. $3\sigma_i$ for SNR = 4 sources. As in C11 we assume that the IR flux and IRAC colour are independent and so $q(S, c) \approx q(S)q(c)$ and similarly $\rho(S, c) \approx \rho(S)\rho(c)$. This assumption is justified, as little correlation is seen between S_{24} or $S_{4.5}$ and $[4.5-3.6]$ colour, with a Spearman rank test giving correlation coefficients of 0.1 and 0.03, respectively.

Fig. 1 shows the probability of finding a source as a function of $S_{4.5}$, S_{24} and $[4.5-3.6]$ within 4 arcsec of a SCUBA-2 450-μm source compared to a random 4 arcsec radius aperture. A clear excess at both IR fluxes and $[3.6-4.5]$ colour can be seen. The integral $q_0 = \int q(S)\,\mathrm{d}S$ gives an estimate of the fraction of counterparts to 450-μm sources we should expect to recover.

[5] http://candels.ucolick.org

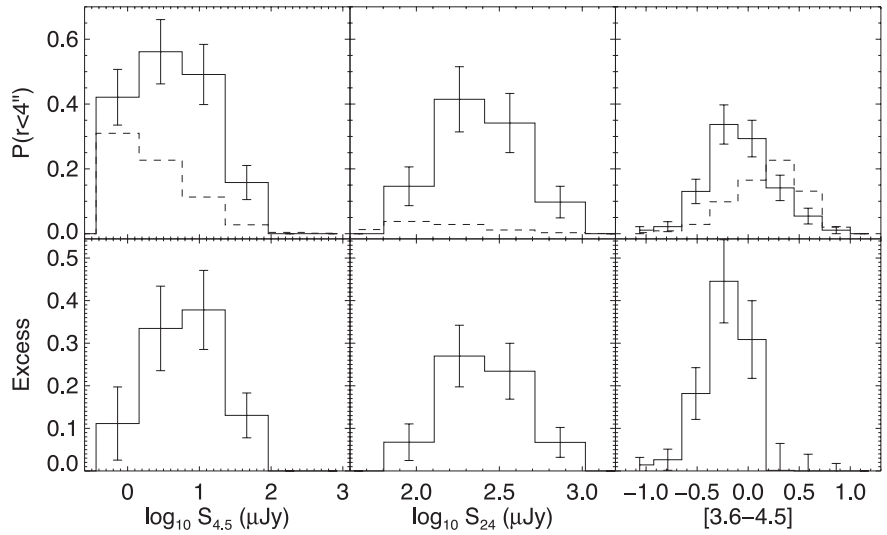

Figure 1. Statistical excess of matching sources as a function of $S_{4.5}$, S_{24} and $[3.6-4.5]$ colour. Top panels: probability of finding a source as a function of $S_{4.5}$ (left), S_{24} (middle) and $[3.6-4.5]$ (right), within 4 arcsec of a SCUBA-2 450-μm source (solid line) or in a random 4 arcsec radius aperture (dashed line). Bottom panels: excess probability of finding a source within 4 arcsec of a 450-μm position.

For the $S_{4.5}$, S_{24} and $[3.6-4.5]$ excess, we find $q_0 = 0.96$, 0.64 and 0.98, respectively. Thus, we would expect almost all of our 450-μm sources to have counterparts above the depth of the matching catalogue ($F160W < 26.5$), and 64 per cent of these to also have 24-μm detections. However, it is worth noting that this assumes that each 450-μm source has a single counterpart, i.e. the 450-μm flux originates from a single, unique, source at 4.5 μm.

In order to determine the false positive rate of cross-identifications, we perform Monte Carlo simulations of the matching process. We generate 10 000 mock source positions at random locations within the SCUBA-2 450-μm field. For each random position, the positional uncertainty is again calculated from the SNR at 450 μm, with the value drawn randomly from the real distribution of observed values. Using the same prior distributions [i.e. $q(S)$ and $q(c)$] as for the real data, we attempt to find identifications in the matching catalogue for these mock sources and calculate the LR of each match.

Using these simulations, we evaluate the false positive rate by taking the ratio of the number of matches in the simulation to the total number of random positions.

Interpolating these simulations, an association has a 20 per cent chance of being spurious at $\log_{10}L = 1.1$. In the COSMOS and UDS fields, 49 and 9 450-μm sources, respectively, have at least one counterpart in the matching catalogues with separation less than 4 arcsec and $\log_{10}L > 1.1$. The vast majority of these have $\log_{10}L \gg 1.1$; taking our measured values of $\log_{10}L$ for each identification, and using our simulations as a guide, we expect 2.3 of our combined total of 58 identifications (4 per cent) to be spurious.

Multiple reliable identifications are found for 11 sources (19 per cent). Given the high reliability of these alternative identifications, it is likely that in these cases the submm flux density is split between the identifications, i.e. both identifications are submm bright and simply blended by the 8 arcsec SCUBA-2 beam. Interestingly, the rate of multiple identifications is similar to the blending rate found for 850-μm-selected samples (e.g. Wang et al. 2011; Karim et al. 2013). For simplicity, we consider the source with the best $\log_{10}L$ value to be the identification and discard the second identification. These alternative identifications are listed in Tables A1 and A2.

4 RESULTS

4.1 Identification statistics and demographics of the 450-μm population

The identification rate of 450-μm sources is 86 ± 12 and 75 ± 25 per cent for the COSMOS and UDS fields, respectively. This leads to a combined identification rate of 84 ± 11 per cent. When compared with our estimate of the potential identification rate from the excess of sources around 450-μm sources, i.e. $q_0 = 0.98$, there is a deficit of 14 per cent, i.e. there are potentially 11 sources which have counterparts in our matching catalogues that could not be reliably recovered by our identification process. Indeed, all of these sources have potential identifications within the maximum search radius (4 arcsec), but are deemed unreliable. However, this deficit may also highlight a weakness in the LR methodology, as it assumes no clustering of the matching catalogue around the 450-μm sources. It is well known that this is not true; in fact, submm sources are strongly clustered (e.g. Karim et al. 2013; Viero et al. 2013) and so q_0 will always be biased.

If we consider only sources with 24-μm identifications above the limits of the surveys considered here (i.e. $S_{24} > 80$ μJy), the rate drops to 65 ± 10 per cent, in good agreement with our estimate from excess sources: $q_0^{24} = 0.64$. This number is important as it is common for *Herschel* photometry to be performed using the prior positions of sources at 24 μm as a guide (e.g. Roseboom et al. 2010). While this approach may be appropriate for brighter flux densities (i.e. $S_{450} > 20$ mJy), or shorter submm wavelengths than we consider here, it is clear from Fig. 2 that at $S_{450} \sim 10$ mJy almost half of the submm sources do not have 24-μm counterparts to a depth of $S_{24} \geq 80$ μJy.

Fig. 2 considers the identification rate as a function of both S_{450} and the submm colour, S_{850}/S_{450}. Interestingly, the identification rate is only modestly dependent on the source flux density, with the overall rate dropping from 87 ± 24 per cent at $S_{450} > 15$ mJy to 82 ± 13 per cent at $5 < S_{450} < 15$ mJy. The effect for 24-μm identifications is larger, falling 11 per cent across the same range.

Only a weak relationship between the submm colour and S_{450} is seen in Fig. 2, with the faintest sources showing some preference for

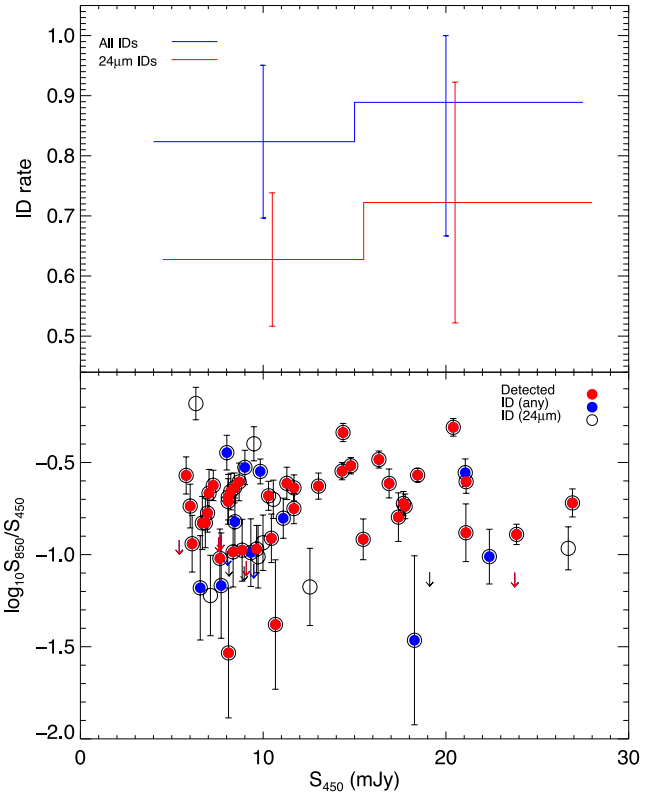

Figure 2. Top: ID rate as a function of the 450-μm flux density. The identification rate is broadly insensitive to S_{450}, with a near-constant level of about 80 per cent for all identifications, and 60 per cent for identifications with $S_{24} > 80$ μJy. Bottom: submm colour (S_{850}/S_{450}) versus 450-μm flux density. The open symbols denote all catalogued 450-μm sources, and those with reliable identifications are shown as filled symbols (blue for all identified, red for 24 μm). Identifications appear insensitive to both the flux density and submm colour, suggesting that our sample is unbiased in terms of redshift and luminosity.

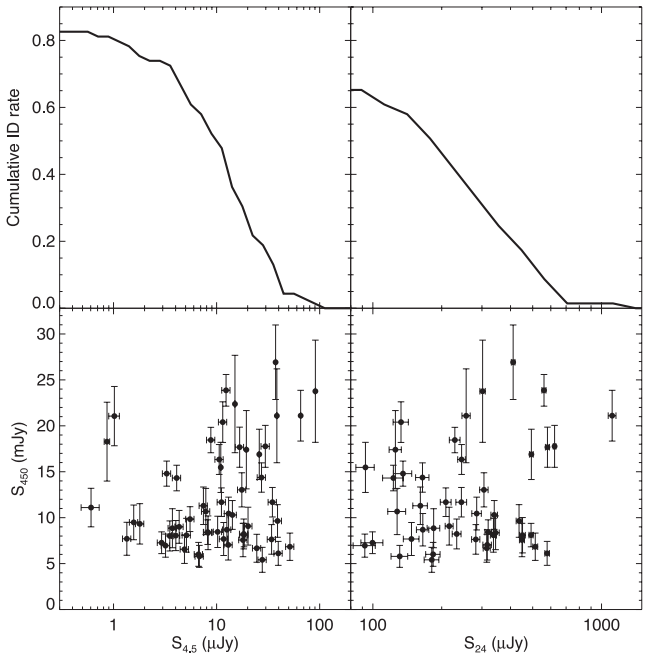

Figure 3. Top panels: cumulative identification rate as a function of decreasing depth for 4.5 μm (left) and 24 μm (right). Bottom panels: matching flux density versus S_{450} for 4.5 μm (left) and 24 μm (right). Both 4.5- and 24-μm flux densities are seen to be weakly correlated with the 450-μm flux density.

bluer submm colours (lower S_{850}/S_{450}). Interestingly, the 11 450-μm sources without reliable identifications do not show any preference in the submm colour. If we consider the colour S_{850}/S_{450} to be a crude tracer of redshift, and combined with the weak dependence of the identification rate on S_{450}, this suggests that our ability to obtain optical/near-IR identifications for our 450-μm sources is independent of both redshift and luminosity.

In Fig. 3, we consider the cumulative identification rate as a function of decreasing flux density at 4.5 and 24 μm, i.e. how deep do ancillary data need to be to return identifications for 450-μm-selected sources? From Fig. 3 we estimate that to return 50 per cent of the identifications would require a depth of $S_{4.5} = 10$ μJy and $S_{24} = 180$ μJy. In the bottom panels of Fig. 3, we show the relationship between $S_{4.5}$, S_{24} and S_{450}. In each case, a weak correlation can be seen, with the brightest 450-μm sources tending to also be bright at 4.5 and 24 μm.

The weak relationship between the 450- and 4.5/24-μm flux densities is intriguing, and potentially worrying, as it may point to a bias away from identifications for the sources with the faintest counterparts. To confirm that the depth of the CANDELS-SCOSMOS/SpUDS data combination is not responsible for either the failure to acquire identifications or a bias towards bright, but erroneous, identifications, we visually inspect the region around each SCUBA-2 source in the deep *Spitzer* Extended Deep Survey 4.5-μm images (Ashby et al. 2013). These images have a completeness of ∼70 per cent at AB mag = 24.25 (0.7 μJy), three times more deeper than IRAC data used here. In none of the 69 sources is there an IRAC source below our current detection limit which is either closer than the current identification or would have a larger LR value. From this analysis, we conclude that our current list of identification is robust, and the 14 sources without identification must either be spurious or simply nightmare cases for the LR methodology (i.e. larger than expected positional offsets, unusual IRAC colours, etc.).

Armed with robust counterparts for more than 80 per cent of our sample, we can investigate the demographics of the 450-μm population. While 58 sources across UDS and COSMOS have reliable identifications, good photometric redshift estimates are only possible for 54 of these; in four cases, the fit to the optical/near-IR photometry is too poor to obtain a reliable photometric redshift estimate (i.e. photo-z $\chi^2 > 20$). Fig. 4 compares the optical/near-IR photometric redshifts for these 54 sources to the submm colour (S_{850}/S_{450}). A weak correlation can be seen, with a Spearman rank correlation coefficient of 0.3 ($p = 0.03$ for no correlation). Also shown in Fig. 4 is the redshift distribution ($\mathrm{d}N/\mathrm{d}z$) for 450-μm sources with $S_{450} > 6$ mJy. To estimate the true $\mathrm{d}N/\mathrm{d}z$, two corrections need to be applied to the observed redshift distribution: (1) a correction for the completeness (and variable depth) of the 450-μm data; and (2) a correction for the incompleteness in identifications/redshifts. The first correction is calculated using the completeness and area estimates from Section 2 specifically; in a given redshift bin the redshift distribution is calculated via $\mathrm{d}N/\mathrm{d}z = \sum_i 1/ca$, where c is the completeness for source i and a is the combined area of the COSMOS and UDS fields. To estimate the redshift distribution of sources without reliable redshift information, we use the weak correlation observed between redshift and S_{850}/S_{450}. For each source without a redshift or identification, we

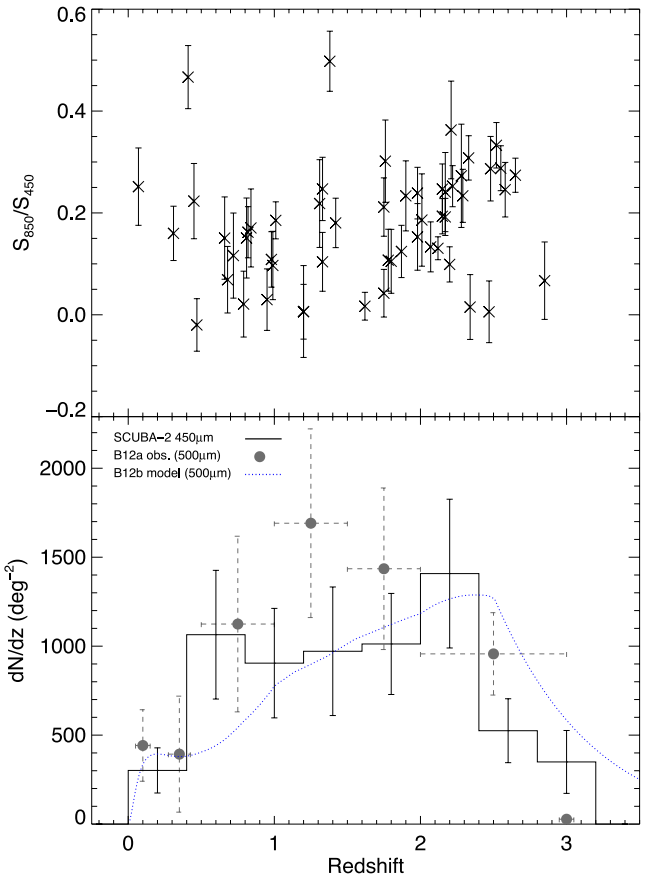

Figure 4. Top: SCUBA-2 submm colour (S_{850}/S_{450}) versus redshift for sources with good identifications and optical/near-IR photometric redshifts. Bottom: redshift distribution (dN/dz) of 450-μm sources. The solid line denotes the dN/dz including corrections for completeness in terms of both 450-μm detection and the identification process. Errors are estimated assuming Poisson statistics. Overplotted as grey points is the equivalent estimate of the dN/dz at SPIRE 500 μm achieved via stacking by Béthermin et al. (2012a, B12a). Also shown is the prediction from the latest evolution model from Béthermin et al. (2012b, B12b). Good agreement is seen between the SCUBA-2 450-μm and both the model and SPIRE 500-μm stacking results.

build a probability distribution $p(z)$ using the redshifts and colours of the identified sample as a guide, i.e. for a source i,

$$p_i(z) = \frac{1}{N\pi\sigma_c} \sum_{j}^{N(z)} \exp\left(-\frac{(c_i - c_j)}{2\sigma_c^2}\right),$$

where the summation runs over the $N(z)$ sources j that fall into a redshift bin centred on z, c_i and c_j are the submm colours of the sources, and $\sigma_c = 0.1$ (the typical error in the submm colour). The submm colours of the non-identified sources are very similar to those with identifications and so the resulting correction to the observed dN/dz is quite flat, i.e. similar to simply multiplying the observed dN/dz by a constant factor at all redshifts.

The redshift distribution of 450-μm sources is broad, peaking in the range $0.5 < z < 2.5$. Few sources are seen at low-z ($z < 0.5$) and high-z ($z > 3$). The overall median of the observed dN/dz is $z = 1.4$, in good agreement with previous work on this data set by Geach et al. (2013), although somewhat lower than the mean of $z = 2$ found for the more luminous 450-μm sample presented in Casey et al. (2013). Reasonable agreement, both in terms of the normalization and shape, is seen between our estimate and both the observed and predicted redshift distribution of SPIRE 500-μm sources from Béthermin et al. (2012a,b). Interestingly, the shape of our dN/dz more closely resembles the Béthermin et al. (2012b, hereafter B12b) model prediction, broad with a peak close to $z = 2.2$, than the Béthermin et al. (2012a, hereafter B12a) result from SPIRE data, which peaks more prominently at $z \sim 1.3$.

We can quantify these comparisons via the use of Kolgmogorov–Smirnov (KS) tests. In the case of the B12b model prediction, we can test directly our SCUBA-2 sample directly, by considering the B12b prediction taking into account the completeness as a function of redshift for our SCUBA-2 catalogue. A KS test suggests an 88 per cent probability that our 450-μm sample is drawn from the B12b model distribution. For the B12a observational result, it is more difficult to apply this type of testing, as the result is derived not from redshifts of individual sources, but from stacking in bins of flux density. Nonetheless, we compare the B12a result to our sample by generating Monte Carlo realizations of the B12a results, taking into account the quoted errors. In each realization, we draw 10 000 galaxies from the B12a distribution and apply the redshift-dependent completeness of our sample. After generating 10 000 realizations, we find that in 40 per cent of realizations a KS test would not distinguish between the two distributions (defined as $p_{\rm KS} > 0.05$). Thus, while the B12a and our dN/dz may appear significantly different in Fig. 4, the significant errors mean that two results are not strictly in conflict.

4.2 Comparing SCUBA-2 and SPIRE photometry

The increased resolution of SCUBA-2 at 450 μm offers the opportunity to assess the impact of the poor angular resolution of SPIRE on photometry at similar submm wavelengths and depths. The SPIRE 500-μm waveband is the most directly comparable as it completely encompasses the SCUBA-2 450-μm bandpass, although with a resolution of 36 arcsec.

variety of methods have been developed to perform photometry at SPIRE wavelengths, which can be broken into two broad classes: those which use prior information at other wavelengths to try to 'deconfuse' the SPIRE photometry (e.g. Roseboom et al. 2010, 2012a) and those which use traditional point source extraction methods without considering other information (e.g. SusseXTractor, SXT; Smith et al. 2012a). In between these methods are a number of 'hybrid' methods, which try to build complete lists of SPIRE sources via point source detection across the SPIRE bands, and then perform photometry at the three wavelengths simultaneously using these detected sources (e.g. Wang et al., in preparation).

Armed with our high-resolution 450-μm data, we can evaluate the effectiveness of these different approaches. To begin, we cross-match our SCUBA-2 450-μm catalogue to three different versions of SPIRE catalogues produced by the HerMES project: the 'XID24' catalogues, which use a *Spitzer* 24-μm prior (Roseboom et al. 2012b); the 'XID250' catalogues, which produce a source list at 250 μm and use these sources as a prior at 500 μm (Wang et al., in preparation); and the SXT catalogues, which simply perform point source detection and extraction at 500 μm (Smith et al. 2012a). The XID24 catalogues are matched to our SCUBA-2 catalogue using a 4 arcsec matching radius between the 450-μm position and the 24-μm position used for the XID24 extraction. The XID250 and SXT catalogues are matched to our SCUBA-2 positions using a 10 arcsec search radius (∼1/3 of the beam FWHM for SPIRE at 500 μm).

For the 69 SCUBA-2 450-μm sources, we find 53 counterparts in the XID24 catalogue, 49 counterparts in the XID250 catalogue and 13 counterparts in the SXT catalogue. For the prior driven

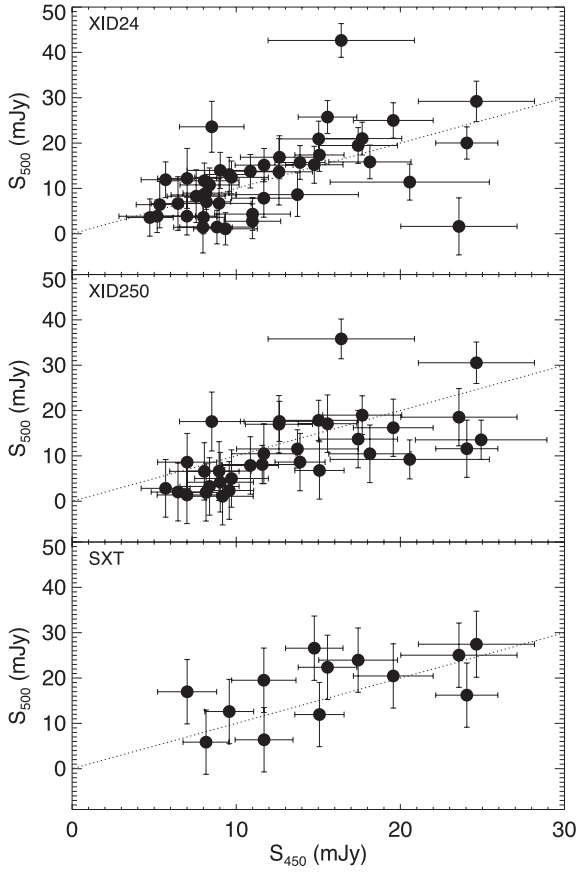

Figure 5. Comparison between SCUBA-2 450-μm and SPIRE 500-μm flux densities for sources in common between our 450-μm catalogue and the HerMES XID24, XID250 and SXT catalogues. For the majority of sources, the XID24 catalogued fluxes agree well with our SCUBA-2 values. The dotted line in each panel shows the one-to-one correspondence. Both the XID250 and SXT catalogues offer worse agreement, with the XID250 values well below the SCUBA-2 measurements at bright ($\gtrsim 20$ mJy) values, while the SXT values show a wide scatter around the SCUBA-2 measurements.

catalogues (i.e. XID24 and XID250), the option exists within the source extraction process to set the 500-μm flux to zero, i.e. the algorithm suggests that no significant 500-μm source is present at this position. Amongst the 53 counterparts in the XID24 catalogue, 44 have non-zero 500-μm flux densities. For the XID250 counterparts, 33 sources have non-zero 500-μm flux densities.

In Fig. 5, we compare the SCUBA-2 450-μm flux densities to the SPIRE 500-μm flux densities for the matched sources in the XID24, XID250 and SXT catalogues. The XID24 flux densities show good agreement with our SCUBA-2 measurements for the majority of sources down to the detection limit for SCUBA-2 ($S_{450} \sim 5$ mJy), with a small number of outliers; only 2 (out of 53; 4 per cent) sources exhibit $|S_{500} - S_{450}|/\Delta S_{500} > 3$. This is an impressive achievement, as the confusion limit (40 beams/src) at 500 μm for SPIRE is about 15 mJy (Nguyen et al. 2010), and so it appears that the use of the 24-μm prior has the ability to produce reliable flux densities well below this limit. The XID250 flux densities show broad agreement with the SCUBA-2 estimates, although they appear to be systematically lower, particularly at bright 450-μm flux density. While SXT flux density estimates only appear for a small number of 450-μm sources, they too show broad agreement, albeit with a large scatter.

5 DISCUSSION

5.1 Submm SEDs

A common way of interpreting submm SEDs is to fit a modified blackbody of the form

$$S_\nu \propto \left\{1 - \exp\left[-\left(\frac{\nu}{\nu_0}\right)^{\beta_\mathrm{D}}\right]\right\} B_\nu(T_\mathrm{D}), \quad (2)$$

where T_D is the dust temperature, ν_0 the rest-frame frequency at which the emission becomes optically thick, β_D is the emissivity and B_ν is the Planck function (e.g. Blain et al. 2003; Magnelli et al. 2012; Roseboom et al. 2012a). It is also common to replace the Wien side of the blackbody SED with a power law at some arbitrary cut-off, i.e. $S_\nu \propto \nu^{-\alpha}$ for ν, where $\frac{\partial S}{\partial \nu} \lesssim -\alpha$. While this type of SED fitting is not very physically motivated, for submm data sets with limited wavelength sampling it offers an effective mechanism for interpolating between the data points (enabling the integrated IR luminosity to be determined), as well as a small set of metrics that crudely describe the shape of the submm SED.

Unfortunately, even this simple parametrization of the SED can be difficult to constrain with typical submm data sets, and so a number of the parameters (generally the emissivity, β_D, the transition frequency, ν_0, and Wien side slope, α) are set to assumed values. This is problematic, as recent studies at low-z are showing that these SED parameters do vary significantly and are a function of the galaxy properties (Auld et al. 2012; Galametz et al. 2012; Smith et al. 2012c). Despite valiant attempts (Chapin et al. 2009; Kovács et al. 2010; Magnelli et al. 2012), typical values for distant galaxies, and their relationship with other properties, are not known.

The shortest observed-frame wavelength considered here is 250 μm, which translates to rest-frame 63 μm at the maximum redshift of our sample ($z = 3$). Thus, our ability to constrain parameters sensitive to the Wien side of the SED (e.g. ν_0, α) is limited. However, the combination of SPIRE and SCUBA-2 does provide excellent coverage of the Rayleigh–Jeans tail of the SED, and so parameters sensitive to this (e.g. β_D) should be well constrained by our data set.

To begin, we select the 23 450-μm sources which have robust ($>3\sigma$) photometry in at least three of the four submm wavebands: SPIRE at 250 and 350 μm and SCUBA-2 at 450 and 850 μm. To these sources, we fit modified blackbody curves (equation 2), allowing L_IR, T_D and β_D to vary, but holding the transition frequency fixed at a rest-frame value of $\nu_0 = c/100$ μm and the Wien side slope to $\alpha = 2$. While these values of ν_0 and α are arbitrary, our results are not highly sensitive to it; repeating our SED fitting with a range of ν_0 values between $\nu_0 = c/50$ and $c/200$ μm, and $\alpha = 1.5$–2.5, changes our estimates of the other SED parameters typically by <10 per cent. The SED fits are performed using a Markov chain Monte Carlo (MCMC) approach which allows both the best-fitting parameter values and variances to be robustly determined. Full details of our MCMC fitting approach are given in Appendix B.

The requirement of good photometry in three bands is effectively an $S_{450} > 11.5$ mJy selection; 19 out of the 23 sources with good photometry have $S_{450} > 11.5$ mJy, while only 2 sources with $S_{450} > 11.5$ mJy are excluded. The vast majority of the 34 sources excluded fail due to having unreliable photometry in the *Herschel* SPIRE bands; this is unsurprising as 11.5 mJy is significantly below the confusion limit for SPIRE (∼18 mJy, 3σ; Nguyen et al. 2010).

Fig. 6 shows the resulting SED fits to the submm photometry. In the majority of cases, the submm SED is well described by

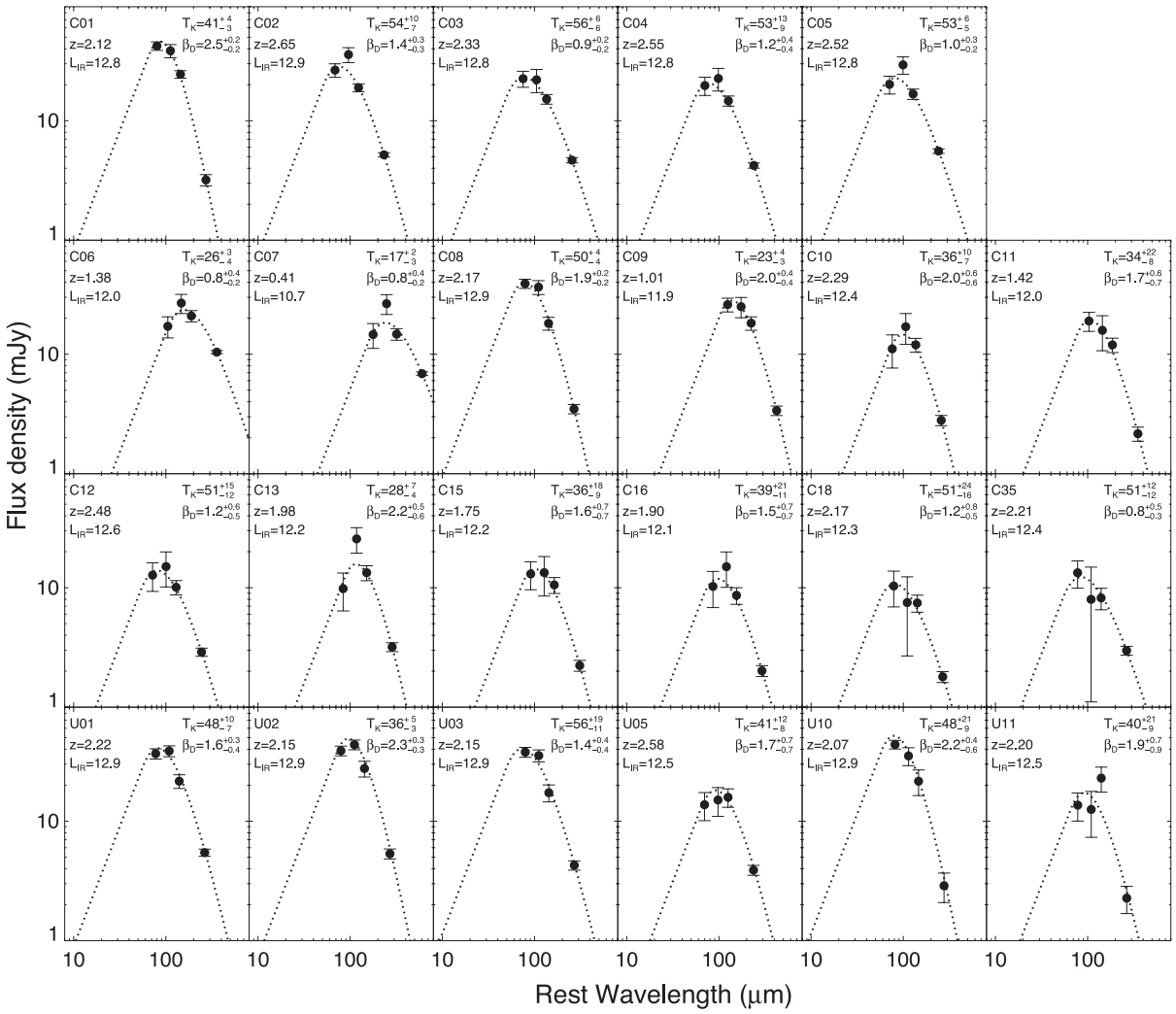

Figure 6. Modified blackbody fits to the submm SEDs for the 23 450-μm sources which have robust photometry in at least three submm bands. In the majority of cases, the modified blackbody offers an excellent description of the submm photometry.

the modified blackbody form. In a number of cases, the SPIRE 350-μm photometry point is inconsistent with the modified blackbody, being a bit higher than the expected value from the fit. We assume that the residual confusion noise in the SPIRE flux extraction is the cause of this discrepancy, which is included in the flux density noise estimates.

To assess how well our limited submm photometry can constrain the modified blackbody parameters, we can use the estimates of the posterior probability distribution for each parameter produced by the MCMC. The typical errors on our estimates of the dust temperature and emissivity (averaging the asymmetric errors) are $\Delta T_{\rm D} = 10\,{\rm K}$ and $\Delta\beta_{\rm D} = 0.4$, respectively, although it is worth noting that these parameters are degenerate, and so the errors are correlated (i.e. increasing $T_{\rm D}$ is degenerate with decreasing $\beta_{\rm D}$; Shetty et al. 2009a). For the mean parameter values, $\langle T_{\rm D}\rangle = 42\,{\rm K}$ and $\langle\beta_{\rm D}\rangle = 1.6$, this translates to an error of ∼20 per cent in both cases. Given this, we can be confident that our submm photometry contains sufficient information to usefully constrain the parameters of the modified blackbody model.

For both the dust temperature and emissivity, the variance in best-fitting parameters is only slightly larger than the typical error, with $\sigma(T_{\rm D}) = 11\,{\rm K}$ and $\sigma(\beta_{\rm D}) = 0.5$. This suggests that assuming single values of the SED parameters would provide a reasonably adequate description of the submm population; the spread in $T_{\rm D}$ and $\beta_{\rm D}$ is small enough that taking a single SED with $T_{\rm D} = 42\,{\rm K}$ and $\beta_{\rm D} = 1.6$ would be sufficient to explain the submm photometry for the majority of our sources. This is illustrated in Fig. 7, which compares the rest-frame, luminosity normalized, photometry for these 23 SCUBA-2 sources to the range in modified blackbody SEDs defined by $T_{\rm D} = 42 \pm 11\,{\rm K}$ and $\beta_{\rm D} = 1.6 \pm 0.5$.

Nonetheless, we consider the possibility that this spread in the SED shape parameters is in part a function of underlying galaxy properties (as opposed to just random scatter). Fig. 8 shows the relationship between the submm SED parameters ($T_{\rm D}$ and $\beta_{\rm D}$) and the galaxy properties: IR luminosity ($L_{\rm IR}$, integrated in the range 8–1000 μm), stellar mass (M_*), dust attenuation (as probed by $L_{\rm IR}/L_{\rm UV}$) and effective radius ($R_{\rm e}$). Stellar mass estimates are made by finding the best fit to the optical/near-IR photometry from a grid of Bruzual & Charlot (2003) templates [solar metallicity; Chabrier (2003) IMF] assuming the photometric redshift as described in Cirasuolo et al. (2010) and Michałowski et al. (2012). The UV luminosity is estimated via λL_λ from a power-law fit to the observed rest-frame UV photometry, with $\lambda = 160\,{\rm nm}$. The effective radius is calculated using the measured R_{50} (i.e. the radius

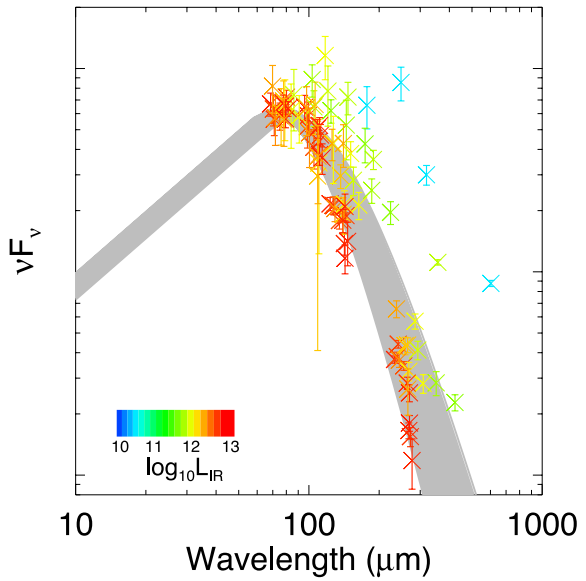

Figure 7. Rest-frame, luminosity normalized, submm photometry for the 23 SCUBA-2 450-μm sources considered here (crosses). Photometric points are colour-coded by $L_{\rm IR}$. Also shown in grey is the range of modified blackbody SED shapes defined by $T_{\rm D} = 42 \pm 11$ K and $\beta_{\rm D} = 1.6 \pm 0.5$. With the exception of a few low-luminosity, low-$T_{\rm D}$, sources, the photometry for most 450-μm population is consistent with this range of SEDs.

which contains 50 per cent of the total light) in the *HST F160W* imaging and the angular diameter distance at the assumed photometric redshift.

Weak correlations between the submm SED shape parameters and some of the galaxy properties can be seen. In order to determine the statistical significance of these correlations, Spearman's rank correlation coefficients are calculated for each of the combinations of submm SED and galaxy properties shown in Fig. 8. These correlation coefficients, and their statistical deviation from the null hypothesis of no correlation, are tabulated in Table 2. Before interpreting these correlations, it is again worth noting that the

Table 2. Spearman's rank correlation coefficients for the relationships between the submm SED shape parameters ($T_{\rm D}$ and $\beta_{\rm D}$) and the galaxy properties, $L_{\rm IR}$, M_* and $R_{\rm e}$. The probability of achieving these correlation coefficients by chance (i.e. the probability of the observed data if no correlation exists) is given in parentheses.

	$T_{\rm D}$	$\beta_{\rm D}$
$L_{\rm IR}$	0.71 (0.001)	0.30 (0.40)
M_*	−0.30 (0.2)	0.49 (0.02)
$L_{\rm IR}/L_{\rm UV}$	0.4 (0.06)	−0.40 (0.06)
$R_{\rm e}$	−0.16 (0.5)	0.41 (0.05)

covariance between $T_{\rm D}$ and $\beta_{\rm D}$ means that we cannot be sure which of these parameters is driving the correlations with other observables, only that the mean submm SED shape is weakly dependent on them.

The IR luminosity, $L_{\rm IR}$, is seen to correlate with $T_{\rm D}$. The existence of the $L_{\rm IR}-T_{\rm D}$ relation has been well documented since *IRAS* (Soifer & Neugebauer 1991; Chapman et al. 2003; Chapin, Hughes & Aretxaga 2009). Recent *Herschel* results show that this relationship extends to high redshift (i.e. $z \sim 2$; Hwang et al. 2010; Magdis et al. 2010; Symeonidis et al. 2013). We compare our estimate of the $L_{\rm IR}-T_{\rm D}$ relation to that determined for local *IRAS* galaxies by Chapin, Hughes & Aretxaga (2009, henceforth CHA09), where we have converted between the *IRAS* colour and $T_{\rm D}$ using equation (2), and fixed values of $c/\nu_0 = 100\,\mu$m and $\beta_{\rm D} = 1.6$. Reasonable agreement is seen between our $L_{\rm IR}-T_{\rm D}$ relation and the CHA09 one, although the 450-μm sources are slightly biased to colder values than the CHA09 relation. This could either be a result of true evolution towards colder dust at high-z (e.g. Seymour et al. 2010) or a bias introduced by requirement of good submm photometry.

Moving on to the stellar mass, a tentative correlation is seen between M_* and $\beta_{\rm D}$. Putting aside the physical implications of such a relation for now, the existence of an $M_*-\beta_{\rm D}$ relation allows us

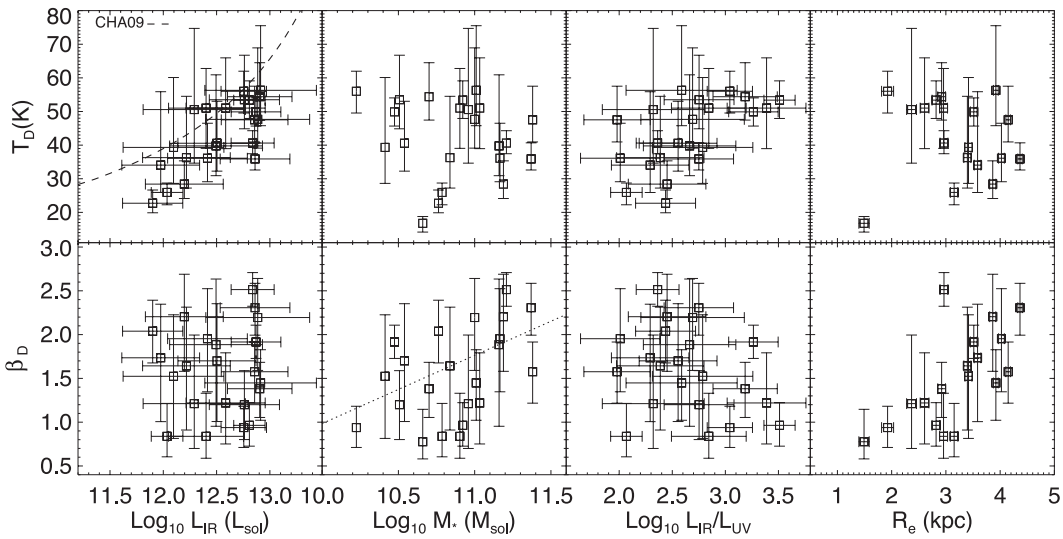

Figure 8. Relationships between submm SED fit parameters and galaxy physical properties. Only those 450-μm sources with reliable 850-μm and SPIRE photometry are considered, leaving a total of 24 submm sources. Correlations between several of the parameters are seen. The best-fitting relation for the $L_{\rm IR}-T_{\rm D}$ relation for *IRAS* galaxies from CHA09 is shown in the top-left panel. The dotted line in the bottom-middle panel shows the best-fitting linear relation found between $\log_{10}M_*$ and $\beta_{\rm D}$.

to predict β_D from a parameter unassociated with the IR SED. We fit a linear relation to $\log_{10}M_*$–β_D, finding a best-fitting relation of $\beta_D = (-7 \pm 2) + (0.8 \pm 0.2)\log_{10}M_*$. This relation will be used later to fix β_D in the SED fits of SCUBA-2 sources that lack reliable submm photometry.

Comparing the dust temperature and emissivity to the dust attenuation, as probed by the ratio of IR to UV luminosity, reveals some weak correlations, with T_D appearing to vary with increasing L_{IR}/L_{UV}, while β_D anticorrelates with attenuation. Both of these correlations are statistically weak, with a Spearman rank $p = 0.06$. Finally, a correlation between the effective radius and β_D is seen, with R_e seen to increase with increasing β_D.

With this information in hand, we now perform SED fits to the remaining 31 SCUBA-2 450-μm sources with reliable identifications and redshifts. The main purpose of this fitting is not to determine parameter values, but merely to have a template with which to estimate the integrated IR luminosity. Again we fit a modified blackbody of the form seen in equation (2), allowing only L_{IR} and T_D to vary, with fixed values for the other parameters: $\nu_0 = c/100\,\mu m$ and $\beta_D = -7 + 0.8\log_{10}M_*$. The IR luminosities ($L_{IR}$) estimated from this fitting, along with all the other galaxy properties, are given in Table A3.

5.2 The potential for a stellar mass – dust emissivity relation

The results shown in Fig. 8 suggest that the shape of the submm SED is somewhat sensitive to the gross properties of the galaxy, with tentative correlations seen between β_D and both stellar mass and size. Interpretation of these correlations is difficult for a number of reasons. First, a single modified blackbody SED is clearly not a complete physical model for the dust emission in a galaxy; a typical star-forming galaxy will contain many distinct star-forming regions enshrouded by dust, as well as more diffuse dust heated by evolved stars, and our observed submm SED is the integrated emission from all of these components. Secondly, the parameters T_D and β_D are known to be degenerate in modified blackbody fits to submm data limited in both wavelength range and SNR (Shetty et al. 2009a,b). Indeed, the 2D posteriors recovered by our MCMC fits for the 23 sources shown in Fig. 8 typically show a correlation coefficient between T_D and β_D of $\sim$−0.9.

However, the existence of this degeneracy between T_D and β_D does not invalidate the conclusion that there may be a relationship between the submm SED shape and both stellar mass and radius. To confirm this, we perform a simple Monte Carlo simulation, taking the measured stellar masses and radii for the 23 sources in Fig. 8 and generating random realizations of T_D and β_D which are imprinted with the covariance found in the MCMC fits to the real data. We produce 10 000 realizations of these simulations and search for correlations of similar strength to those seen in the real data. As expected, the incidence of correlations at the strength quoted in Table 2 is close to what would be predicted analytically: $p = 0.017 \pm 0.001$ for the M_*–β_D relation and $p = 0.044 \pm 0.001$ for the R_e–β_D relation.

Thus, while the correlations between the SED shape and both stellar mass and effective radii may be real, to observationally discriminate which of the SED parameters is driving this relationship would require the individual star-forming regions to be resolved at a wide range of far-IR and submm wavelengths, something that not even ALMA will be capable of for these distant galaxies. However, we can check if this behaviour is also seen in resolved studies of nearby galaxies with *Herschel*. Galametz et al. (2012) present a detailed analysis of the dust temperature and emissivity distribution observed within 11 local galaxies using data from the *Herschel* KINGFISH survey (Kennicutt et al. 2011). By fitting single modified blackbody SEDs to individual pixels in the *Herschel* images, they find a wide range of dust temperatures and emissivities within galaxies. In many cases, a trend of decreasing dust temperature and emissivity is seen with radius. These trends are also seen in *Herschel* observations of M31 (Smith et al. 2012c). Again these studies are subject to the same caveats about T_D–β_D degeneracies, although the resolved nature of the observations, as well as the increased SNR, alleviates some of these concerns.

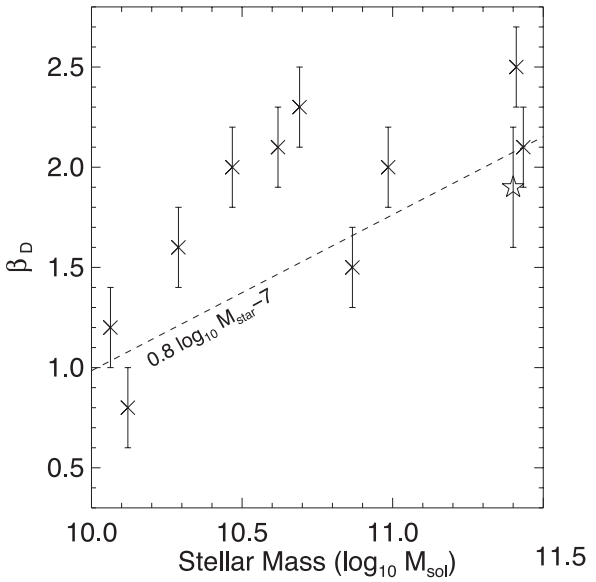

Figure 9. Dust emissivity versus stellar mass for local galaxies in the KINGFISH sample (crosses; Galametz et al. 2012) and M31 (star; Smith et al. 2012c). Overplotted is the M_*–β_D relation seen in our SCUBA-2 sample in Fig. 8.

If we take the median emissivity values for the KINGFISH sample (table 3 of Galametz et al. 2012) and M31 (Smith et al. 2012c) and compare these to the stellar masses for these local galaxies (estimated from the published K_s magnitudes and assuming $M_*/L_{K_s} = 0.8$; Bell et al. 2003; Munoz-Mateos et al. 2009), we again see a trend of dust emissivity increasing with stellar mass. This is shown in Fig. 9. The emissivity–stellar mass relation for local, resolved, galaxies is nearly identical to the one we see for distant 450-μm-selected sources. This should not be taken as evidence for a real physical link between these parameters, merely that the submm SED shape for both local and distant (i.e. $z > 1$) galaxies responds in a similar way to changes in the stellar mass.

5.3 The sSFR of 450-μm sources

The primary utility of deep submm imaging is as an unambiguous tracer of SFR. The ability to probe rest-frame wavelengths longward of 100 μm is particularly valuable for distant galaxies as it is difficult for physical processes other than star formation (i.e. AGN, diffuse ISM dust) to be responsible for the highly luminous, but still cold, thermal emission observed (e.g. Fig. 6). This allows us to convert our integrated IR luminosities into SFRs without reservation, using the relation of Kennicutt et al. (1998), after converting to a Chabrier (2003) IMF, $\log_{10}(\mathrm{SFR/M_\odot\ yr^{-1}}) = \log_{10}(L_{IR}/L_\odot) - 10$.

In Fig. 10, we plot the SFR estimates for our SCUBA-2 450-μm sources against redshift. Our SCUBA-2 data set is clearly limited to SFRs of greater than 10 $M_\odot$ yr^{-1} at $z = 1$ and 100 $M_\odot$ yr^{-1} at

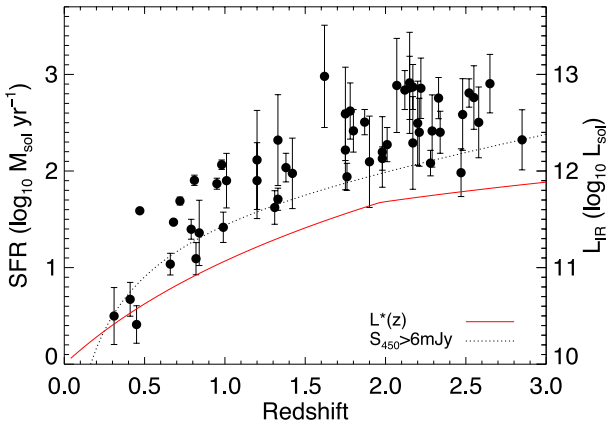

Figure 10. SFR versus redshift for SCUBA-2 450-μm sources. The dotted line shows the expected minimum SFR (L_{IR}) as a function of redshift, assuming a modified blackbody SED with the mean parameters from Section 5.1 (i.e. $T_D = 42$ K, $\beta_D = 1.6$). The solid red line shows $L^*(z)$ as estimated by Gruppioni et al. (2013).

$z = 2$. It is interesting to compare these limits to the evolution of the knee of the IR luminosity function, L^*. Also shown in Fig. 10 is the evolution of L^* with redshift as estimated by Gruppioni et al. (2013). Because of the combined effect of the negative K-correction and strong evolution in the IR luminosity function, the SCUBA-2 450-μm sensitivity limit is only slightly, although consistently, above $L^*(z)$ with a difference of 0.3 dex, i.e. a factor of roughly 2 for $z > 0.5$.

Thus, with our current SCUBA-2 data set, we are not able to individually detect 'typical' galaxies at high redshift. However, the small separation between our sensitivity limits and $L^*(z)$, and the quality of the ancillary CANDELS data in our S2CLS fields, means that the aggregate SFRs of galaxies at all redshifts should be easily obtainable via stacking techniques.

In both the UDS and COSMOS fields, we take the full $F160W < 25$ AB mag CANDELS catalogues with photometric redshifts and stellar mass estimates. These catalogues are split by both redshift and mass into six bins described in Table 3. Passive galaxies are excluded by requiring that the rest-frame NUV$-r < 3.5$, as per Karim et al. (2011).

Table 3 gives the numbers of sources and mean quantities for these six bins. Stacking is performed in the four submm bands available, using the method described in Appendix C. Estimates on the variance in the stacked quantities are calculated by jack knifing the input catalogue.

Fig. 11 compares the SFR to the stellar mass for both individual galaxies in our 450-μm sample and our stacked quantities. Shown for comparison in Fig. 11 are the mean SFR–M_* relations seen for star-forming galaxies at a variety of redshifts via stacking in the

Table 3. Details of z–M_* bins used to stack the submm imaging.

z	M_* ($\log_{10}$ $M_\odot$)	N_{src}	$\langle L_{IR} \rangle$ ($\log_{10}$ $L_\odot$)
$0 < z < 1.5$	<10 ⟨9.0⟩	4466	9.8 ± 0.2
$0 < z < 1.5$	10...10.5 ⟨10.2⟩	314	11.3 ± 0.1
$0 < z < 1.5$	>10.5⟨10.7⟩	163	11.5 ± 0.2
$1.5 < z < 3$	<10 ⟨9.7⟩	2270	9.6 ± 1.0
$1.5 < z < 3$	10...10.5 ⟨10.2⟩	527	11.6 ± 0.2
$1.5 < z < 3$	>10.5 ⟨10.7⟩	406	11.8 ± 0.2

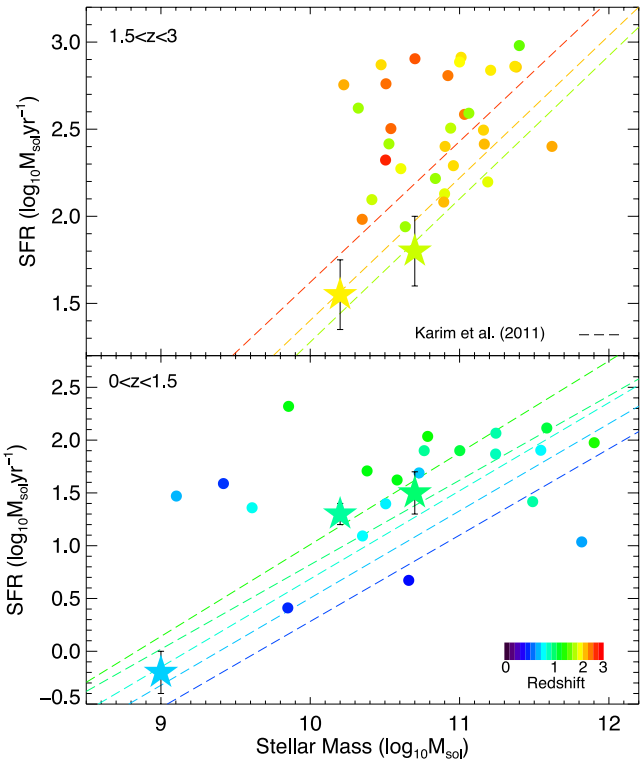

Figure 11. SFR versus stellar mass for 450-μm sources. Sources are split into two redshift bins ($0 < z < 1.5$ and $1.5 < z < 3$) and colour-coded by redshift. Individual sources detected at 450 μm are shown as filled circles, while results from stacking the submm data of near-IR-selected galaxies in mass and redshift bins are shown as filled stars. Shown for comparison is the mean SFR–M_* relation for star-forming galaxies as a function of redshift from Karim et al. (2011).

radio (Karim et al. 2011). In general, our stacked results show good agreement with the Karim et al. (2011) SFR–M_* relation, or typical specific SFR (sSFR: SFR/M_*) at a given redshift. Meanwhile the individually detected 450-μm sources tend to lie above this, a result of the limited sensitivity of, and the small volume probed by, our sample.

In recent years, the dispersion around the SFR–M_* relation has become a quantity of much interest, as the existence of a distinct population of 'starbursts' with exceptionally high sSFR has been postulated. Using parametric fits to the spread in the SFR–M_*, Rodighiero et al. (2011) suggest that the 'main-sequence' population (i.e. those galaxies consistent with the SFR–M_* relation) can be described by a Gaussian distribution with $\sigma = 0.25$ dex plus a population of excess 'starbursts' observed at +0.6 dex.

Using the same definition for starbursts here, we identify those individual 450-μm sources which have an sSFR +0.6 dex, or more, greater than the stacked sSFR at comparable redshift and mass. Of the 54 sources considered, only 14 are classified as starbursts (26 per cent). This fraction is reasonably consistent across the two redshift bins, with 5/23 (22 per cent) starbursts in the low-z bin and 9/31 starbursts (29 per cent) in the high-z bin. Rodighiero et al. (2011) estimate that the starburst fraction is 20–30 per cent for samples limited to SFR $\gtrsim 100\,M_\odot\,yr^{-1}$, in good agreement with our estimate.

However, this definition for a population of excess sSFR starbursts is somewhat arbitrary, and highly sensitive to the assumed location, and width, of the SFR–M_* relation. While our data are not substantial enough to perform parametric fits to the full

SFR–M_* space, we can ask whether the sSFR values determined for our individual sources, in combination with our stacking results, are consistent with a single unimodal distribution.

For each 450-μm source, we estimate the mean sSFR at its redshift and mass by extrapolating from our stacked sSFR values, and assuming the mean slope of the SFR–M_* found by Karim et al. (2011), i.e. SFR $\propto M_*^{0.4}$. As our sample covers a wide range in redshift, across which the mean SFR–M_* relation and our sensitivity to $L_{\rm IR}$ are varying, it is difficult to correct our sample for completeness in terms of distance from the SFR–M_* relation, i.e. ΔsSFR. To avoid issues of incompleteness in terms of the stellar mass, we consider only the 47 sources with $M_* > 10^{10}\,{\rm M}_\odot$. However, we can crudely estimate an sSFR at which our sample becomes complete using the results of Figs 10 and 11. In the redshift range $0 < z < 1.5$, our limiting SFR is $>40\,{\rm M}_\odot\,{\rm yr}^{-1}$, while at $1.5 < z < 3$ it is $>160\,{\rm M}_\odot\,{\rm yr}^{-1}$. Given our stacking results, the mean sSFRs for $M_* = 10^{10.2}\,{\rm M}_\odot$ galaxies are 0.1 and 0.4 ${\rm Gyr}^{-1}$ for the low- and high-z bins, respectively. Taking our estimated SFR limits and the mean stellar mass in these bins ($10^{10.2}\,{\rm M}_\odot$), our limiting sSFRs are ∼0.4 and ∼1 ${\rm Gyr}^{-1}$. So we can expect that we are roughly complete in terms of ΔsSFR at >0.3 in the low-z bin and >0.6 in the high-z bin, i.e. below the threshold of +0.6 dex for starbursts set by Rodighiero et al. (2011).

For galaxies with $M_* > 10^{10}\,{\rm M}_\odot$, we observe nine with an sSFR excess of +0.6 dex or more. A Gaussian distribution with $\sigma = 0.25$ dex normalized to the total number of $M_* > 10^{10}\,{\rm M}_\odot$ predicts that we should observe six, so our result represents an $\sim 1\sigma$ excess assuming Poisson statistics. While we are clearly limited by our small sample, we do not find any evidence that these high-sSFR galaxies belong to a distinct population from the general population of star-forming galaxies. It is worth noting that at the mass limit considered here (i.e. $M_* > 10^{10.5}\,{\rm M}_\odot$), Rodighiero et al. (2011) find significantly smaller numbers of high-sSFR galaxies than at lower masses. It may be that the starburst phenomenon is more prevalent at masses lower than we can reasonably probe here.

Another way to test the sSFR starburst hypothesis is to look for correlations between the sSFR and other galaxy properties. In Fig. 12, we compare the galaxy properties considered here that are unrelated to sSFR (i.e. $R_{\rm e}$, $L_{\rm IR}/L_{\rm UV}$ and $T_{\rm D}$) for 'starburst' (i.e. ΔsSFR > 0.6 dex) and normal star-forming galaxies. While there are some hints of differences, with starbursts potentially hotter and experiencing more dust attenuation (i.e. higher $L_{\rm IR}/L_{\rm UV}$), these differences are not statistically significant; KS tests suggest that all of these distributions are consistent at the $p = 0.5$ level or better. While this may be a result of the small sample size considered here, some larger studies also fail to find significant trends between the location in the SFR–M_* plane and galaxy properties. Law et al. (2012) considered 306 distant galaxies with *HST* WFC3 and found no morphological dependence on the sSFR. Taking samples of close pairs from $0 < z < 1$, Xu et al. (2012) found no evidence for an increase in sSFR for interactions versus normal isolated disc galaxies at $z \sim 1$, with a preference for interactions to have high sSFR only seen at low-z. Near-IR integral field unit studies also fail to find a connection between internal kinematics (i.e. rotation or dispersion dominated) and being on or off the 'main sequence' (Förster-Schreiber et al. 2009).

This connection (or lack of) between the sSFR and galaxy properties is important for a number of reasons. The dominance of the SFR–M_* relation has been taken as evidence that the influence of mergers in galaxy formation is minor (Rodighiero et al. 2011). However, there is no clear observational evidence that galaxy–galaxy mergers should lie above the SFR–M_* relation. Modern hydrodynamical simulations suggest that while mergers can boost SFR,

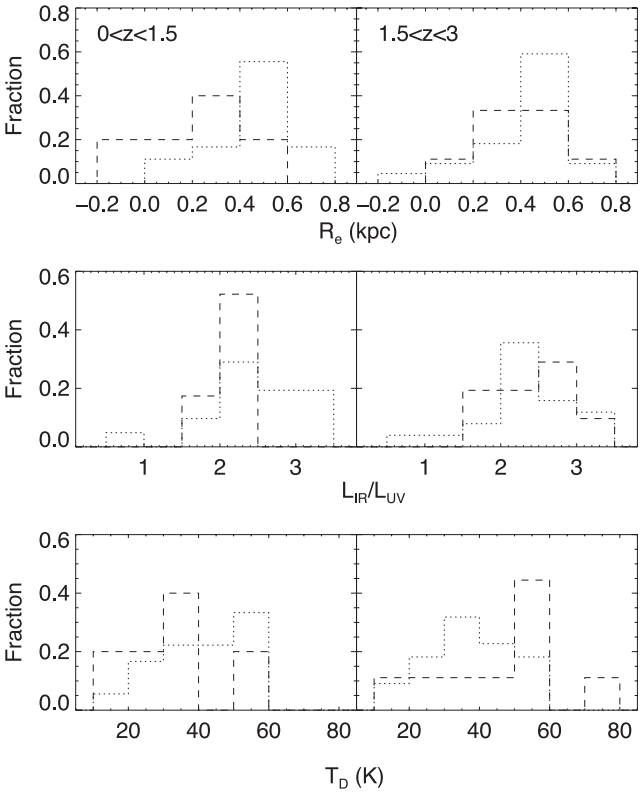

Figure 12. Distribution of galaxy properties for starburst (dashed) and normal star-forming (dotted) galaxies.

these enhancements may only be modest in some cases (i.e. a factor of 2) and occur over time-scales significantly shorter than the observational merger signatures (Di Matteo et al. 2008; Bournaud et al. 2011; Hayward et al. 2012). For these reasons, using sSFR as a tracer for the number of merger-induced starbursts is flawed; while high values of sSFR may be exclusively merger driven, not all observed mergers will have high sSFR. This distinction is also consistent with the discrepancy between the fraction of high-sSFR starbursts (∼2 per cent) and the global merger rate at $z \sim 2$ (10–20 per cent; Conselice et al. 2000; Lotz et al. 2011; Bluck et al. 2012; Law et al. 2012). Future resolved observations of distant galaxies with facilities like ALMA will likely determine if the sSFR of galaxies is indeed a signature of merger-induced star formation.

6 CONCLUSIONS

We have presented a detailed investigation into the multiwavelength properties of 69 450-μm sources selected from two fields (COSMOS and UDS) from the S2CLS. These data represent the first 10 months of observing for S2CLS and reach a depth of ∼1.5 mJy rms at 450 μm in the deepest regions. Using LR techniques, we found robust optical/near-IR counterparts from overlapping *HST* CANDELS data for 58 (84 per cent) of these sources. Focusing on this sample of robustly identified sources, we were able to reach the following conclusions.

(i) The redshift distribution of 450-μm sources with $S_{450} \gtrsim 6$ mJy was estimated, with a broad peak in ${\rm d}N/{\rm d}z$ seen within $1 < z < 3$ and an overall median of $z = 1.4$. Few 450-μm sources are found to lie at very high redshifts (i.e. $z > 3$). While the 26 per cent of sources without identifications could lie at preferentially higher redshifts,

their submm flux densities and colours suggest that they are not distinct from the sources with identifications.

(ii) By fitting modified blackbody SEDs to the combined *Herschel* SPIRE and SCUBA-2 photometry, the range and physical dependence of SED properties on galaxy properties were investigated. Using an MCMC fitting technique, and allowing both the dust temperature ($T_{\rm D}$) and emissivity ($\beta_{\rm D}$) to vary, we found the mean values for these parameters for our 450-μm sample ($\langle L_{\rm IR}\rangle = 10^{12}\,{\rm L}_{\odot}$) to be $\langle T_{\rm D}\rangle = 42 \pm 11$ K and $\langle \beta_{\rm D}\rangle = 1.6 \pm 0.5$. Comparing these SED parameters, clear evidence of the well-known $L_{\rm IR}-T_{\rm D}$ relation was observed, while new weak correlations between $\beta_{\rm D}$ and both stellar mass and effective radius were discovered. These relations all appear to be similar to those observed for local galaxies.

(iii) The relationship between the SFR and stellar mass was investigated, with the majority (74 per cent) of 450-μm sources found to be consistent with previous measures of the SFR–M_* relation (e.g. Karim et al. 2011). Apart from their sSFR, these 'starburst' galaxies are indistinguishable from the galaxies on the SFR–M_* relation, although this may be a result of the limited diagnostic power of the multiwavelength data we possess for these sources.

When completed, S2CLS will possess deep ($\sigma_{450} \sim 1$ mJy) 450-μm imaging over 0.6 deg^2, a factor of almost 10 over the area used in this work. All of these data will have overlapping multiwavelength coverage similar to that available for the fields studied here. On the basis of our results, the potential for 450-μm imaging from S2CLS is clear; a large sample (∼600) of submm-selected galaxies with exquisite SED information from the optical through to submm will allow detailed questions about the nature of dust and the role of starbursts in distant galaxies to be addressed in a way not previously possible, and likely to be unsurpassed until the arrival of large-scale ALMA surveys and new single-dish facilities like Large Millimeter Telescope and Cornell Caltech Atacama Telescope (Hughes et al. 2010; Woody et al. 2012).

ACKNOWLEDGEMENTS

We thank the anonymous referee for suggestions which greatly enhanced this work.

We also thank B. Sidthorpe and W. Holland for many useful discussions related to the reduction and analysis of SCUBA-2 imaging.

JSD acknowledges the support of the Royal Society via a Wolfson Research Merit award and the support of the European Research Council via the award of an Advanced Grant.

IRS acknowledges support from STFC (ST/I001573/1), a Leverhulme Fellowship, the ERC Advanced Investigator programme DUSTYGAL and a Royal Society/Wolfson Merit Award.

LW and SJO were supported by the Science and Technology Facilities Council (grant number ST/I000976/1).

Many thanks to the JCMT telescope operators: J. Hoge, J. Wouterloot and W. Montgomerie, without whom these observations would not be possible.

The James Clerk Maxwell Telescope is operated by the Joint Astronomy Centre on behalf of the Science and Technology Facilities Council of the United Kingdom, the National Research Council of Canada and (until 2013 March 31) the Netherlands Organisation for Scientific Research. Additional funds for the construction of SCUBA-2 were provided by the Canada Foundation for Innovation.

SPIRE has been developed by a consortium of institutes led by Cardiff Univ. (UK), including Univ. Lethbridge (Canada); NAOC (China); CEA, LAM (France); IFSI, Univ. Padua (Italy); IAC (Spain); Stockholm Observatory (Sweden); Imperial College London, RAL, UCL-MSSL, UKATC, Univ. Sussex (UK); and Caltech, JPL, NHSC, Univ. Colorado (USA). This development has been supported by national funding agencies: CSA (Canada); NAOC (China); CEA, CNES, CNRS (France); ASI (Italy); MCINN (Spain); SNSB (Sweden); STFC, UKSA (UK); and NASA (USA). All the data used in this analysis are available through the JCMT, *Herschel, HST* and *Spitzer* archives.

REFERENCES

Alaghband-Zadeh S. et al., 2012, MNRAS, 424, 2232
Amblard A. et al., 2011, Nat, 470, 510
Ashby M. L. N. et al., 2013, ApJ, 769, 80
Auld R. et al., 2012, MNRAS, 420, 1882
Austermann J. E. et al., 2010, MNRAS, 401, 160
Barger A. J., Cowie L. L., Sanders D. B., Fulton E., Taniguchi Y., Sato Y., Kawara K., Okuda H., 1998, Nat, 394, 248
Béthermin M., Dole H., Lagache G., Le Borgne D., Penin A., 2011, A&A, 529, A4
Béthermin M. et al., 2012a, A&A, 542, A58 (B12a)
Béthermin M. et al., 2012b, ApJ, 757, L23 (B12b)
Blain A. W., Barnard V. E., Chapman S. C., 2003, MNRAS, 338, 733
Bluck A. F. L., Conselice C. J., Buitrago F., Grützbauch R., Hoyos C., Mortlock A., Bauer A. E., 2012, ApJ, 747, 34
Bournaud F. et al., 2011, ApJ, 730, 4
Bowler R. A. A. et al., 2012, MNRAS, 426, 2772
Bruzual G., Charlot S., 2003, MNRAS, 344, 1000
Casey C. M. et al., 2013, preprint (arXiv:1302.2619)
Chabrier G., 2003, PASP, 115, 763
Chapin E. L. et al., 2009, MNRAS, 398, 1793
Chapin E. L. et al., 2011, MNRAS, 411, 505 (C11)
Chapin E. L., Hughes D. H., Aretxaga I., 2009, MNRAS, 393, 653
Chapin E. L., Berry D. S., Gibb A. G., Jenness T., Scott D., Tilanus R. P. J., Economou F., Holland W. S., 2013, MNRAS, 430, 2545
Chapman S. C., Helou G., Lewis G. F., Dale D. A., 2003, ApJ, 588, 186
Chapman S. C., Blain A. W., Smail I., Ivison R. J., 2005, ApJ, 622, 772
Chary R.-R., Cooray A., Sullivan I., 2008, ApJ, 681, 53
Cirasuolo M., McLure R. J., Dunlop J. S., Almaini O., Foucaud S., Simpson C., 2010, MNRAS, 401, 1166
Clements D. L. et al., 2010, A&A, 518, L8
Conselice C. J., Bershady M. A., Jangren A., 2000, ApJ, 529, 886
Cooray A. et al., 2010, A&A, 518, L22
Daddi E. et al., 2007, ApJ, 670, 156
Dempsey J. T. et al., 2013, MNRAS, 430, 2534
Di Matteo P., Bournaud F., Martig M., Combes F., Melchior A.-L., Semelin B., 2008, A&A, 492, 31
Diolaiti E., Bendinelli O., Bonaccini D., Close L., Currie D., Parmeggiani G., 2000, A&AS, 147, 335
Eales S. et al., 2010, PASP, 122, 499
Elbaz D. et al., 2007, A&A, 468, 33
Elbaz D. et al., 2010, A&A, 518, L29
Farrah D. et al., 2001, MNRAS, 326, 1333
Förster-Schreiber N. M. et al., 2009, ApJ, 706, 1364
Förster-Schreiber N. M., Shapley A. E., Erb D. K., Genzel R., Steidel C. C., Bouché N., Cresci G., Davies R., 2011, ApJ, 731, 65
Galametz M. et al., 2012, MNRAS, 425, 763
Geach J. E. et al., 2013, MNRAS, 432, 53
Gelman A., Rubin D. B., 1992, Stat. Sci., 7, 457
Glenn J. et al., 2010, MNRAS, 409, 109
Griffin M. J. et al., 2010, A&A, 518, L3
Grogin N. A. et al., 2011, ApJS, 197, 35
Gruppioni C. et al., 2013, MNRAS, 432, 23
Hainline L. J., Blain A. W., Smail I., Alexander D. M., Armus L., Chapman S. C., Ivison R. J., 2011, ApJ, 740, 96
Hayward C. C., Jonsson P., Kereš D., Jonsson P., KeresŽ D., Magnelli B., Hernquist L., Cox T. J., 2012, MNRAS, 424, 951

Holland W. S. et al., 2013, MNRAS, 430, 2513
Hughes D. H. et al., 1998, Nat, 394, 241
Hughes D. H. et al., 2010, in Stepp L. M., Gilmozzi R., Hall H. J., eds, Proc. SPIE Vol. 7733, The Large Millimeter Telescope. SPIE, Bellingham, p. 773312
Hwang H. S. et al., 2010, MNRAS, 409, 75
Ivison R. J. et al., 2007, MNRAS, 380, 199
Karim A. et al., 2011, ApJ, 730, 61
Karim A. et al., 2013, MNRAS, 432, 2
Kennicutt R. C., Jr, 1998, ARA&A, 36, 189
Kennicutt R. C. et al., 2011, PASP, 123, 1347
Koekemoer A. M. et al., 2011, ApJS, 197, 36
Kovács A. et al., 2010, ApJ, 717, 29
Kurczynski P., Gawiser E., 2010, AJ, 139, 1592
Law D. R., Steidel C. C., Shapley A. E., Nagy S. R., Reddy N. A., Erb D. K., 2012, ApJ, 745, 85
Le Floćh E. et al., 2009, ApJ, 703, 222
Levenson L. et al., 2010, MNRAS, 409, 83
Lilly S. J. et al., 2007, ApJS, 172, 70
Lotz J. M., Jonsson P., Cox T. J., Croton D., Primack J. R., Somerville R. S., Stewart K., 2011, ApJ, 742, 103
Madau P., Ferguson H. C., Dickinson M. E., Dickinson M. E., Giavalisco M., Steidel C. C., Fruchter A., 1996, MNRAS, 283, 1388
Maddox S. J. et al., 2010, A&A, 518, L11
Magdis G. E. et al., 2010, MNRAS, 409, 22
Magnelli B. et al., 2012, A&A, 539, A155
Marsden G. et al., 2009, ApJ, 707, 1729
Michałowski M., Hjorth J., Watson D., 2010, A&A, 514, A67
Michałowski M. J., Dunlop J. S., Cirasuolo M., Hjorth J., Hayward C. C., Watson D., 2012, A&A, 541, A85
Mihos J. C., Hernquist L., 1994, ApJ, 431, L9
Mortier A. M. J. et al., 2005, MNRAS, 363, 563
Nguyen H. T. et al., 2010, A&A, 518, L5
Noeske K. G. et al., 2007, ApJ, 660, L43
Oliver S. J. et al., 2010, A&A, 518, L21
Oliver S. J. et al., 2012, MNRAS, 424, 1614
Pilbratt G. L. et al., 2010, A&A, 518, L1
Reddy N. A., Steidel C. C., Erb D. K., Shapley A. E., Pettini M., 2006, ApJ, 653, 1004
Rodighiero G. et al., 2011, ApJ, 739, L40
Roseboom I. G. et al., 2010, MNRAS, 409, 48
Roseboom I. G. et al., 2012a, MNRAS, 419, 2758 (R12)
Roseboom I. G. et al., 2012b, MNRAS, 426, 1782
Sanders D. B., Soifer B. T., Elias J. H., Madore B. F., Matthews K., Neugebauer G., Scoville N. Z., 1988, ApJ, 325, 74
Seymour N., Symeonidis M., Page M. J., Huynh M., Dwelly T., McHardy I. M., Rieke G., 2010, MNRAS, 402, 2666
Shetty R., Kauffmann J., Schnee S., Goodman A. A., 2009a, ApJ, 696, 676
Shetty R., Kauffmann J., Schnee S., Goodman A. A., Ercolano B., 2009b, ApJ, 696, 2234
Smail I., Ivison R. J., Blain A. W., 1997, ApJ, 490, L5
Smith A. J. et al., 2012a, MNRAS, 419, 377
Smith D. J. B. et al., 2012b, MNRAS, 427, 703
Smith M. W. L. et al., 2012c, ApJ, 756, 40
Soifer B. T., Neugebauer G., 1991, AJ, 101, 354
Sutherland W., Saunders W., 1992, MNRAS, 259, 413
Swinbank A. M. et al., 2010, MNRAS, 405, 234
Symeonidis M. et al., 2013, MNRAS, 431, 2317
Targett T. A., Dunlop J. S., McLure R. J., Best P. N., Cirasuolo M., Almaini O., 2011, MNRAS, 412, 295
Targett T. A. et al., 2013, MNRAS, 432, 2012
van Kampen E. et al., 2012, MNRAS, 426, 3455
Viero M. P. et al., 2013, ApJ, 772, 77
Wang W.-H., Cowie L. L., Barger A. J., Williams J. P., 2011, ApJ, 726, L18
Weiß A. et al., 2009, ApJ, 707, 1201
Woody D. et al., 2012, Proc. SPIE Vol. 8444, Ground-based and Airborne Telescopes IV. SPIE, Bellingham, p. 84442M
Xu C. K. et al., 2012, ApJ, 760, 72

APPENDIX A: SCUBA-2 450-μm SOURCE CATALOGUES

Table A1. 450-μm sources in the COSMOS CANDELS region. Sources with only unreliable identifications (i.e. $\log_{10}LR < 1.1$) are shown in italics. Where multiple good identifications for sources exist, these are listed with the suffix.2,.3, etc.

ID	RA_{450} (°)	$Dec._{450}$ (°)	S_{450} (mJy)	ΔS_{450} (mJy)	SNR_{450}	S_{850} (mJy)	ΔS_{850} (mJy)	RA_{opt} (°)	$Dec._{opt}$ (°)	Sep. (arcsec)	$\log_{10}LR$	z_{phot}
S2CLSc01	150.1638	2.3721	24.46	1.77	13.72	3.19	0.34	150.163 57	2.372 42	1.38	4.16	2.12
S2CLSc02	150.1055	2.3125	18.91	1.42	13.13	5.18	0.21	150.105 46	2.312 85	1.09	4.12	2.65
S2CLSc03	150.1430	2.3556	15.17	1.40	10.55	4.67	0.23	150.143 04	2.355 85	0.89	3.90	2.33
S2CLSc04	150.0985	2.3207	14.67	1.43	10.06	4.22	0.22	150.098 66	2.320 81	0.87	3.91	2.55
S2CLSc04.2	150.0985	2.3207	14.67	1.43	10.06	4.22	0.22	150.099 14	2.320 69	2.46	2.12	1.03
S2CLSc05	150.0989	2.3649	16.74	1.67	9.83	5.57	0.24	150.098 54	2.365 36	1.99	3.53	2.52
S2CLSc06	150.0655	2.2636	20.91	2.27	8.98	10.41	0.32	150.064 60	2.264 05	3.59	1.17	1.38
S2CLSc07	150.1000	2.2971	14.73	1.64	8.79	6.87	0.24	150.100 14	2.297 13	0.55	3.47	0.41
S2CLSc08	150.1065	2.2516	18.11	2.24	8.00	3.48	0.31	150.106 41	2.251 61	0.37	4.62	2.17
S2CLSc08.2	150.1065	2.2516	18.11	2.24	8.00	3.48	0.31	150.106 35	2.251 10	1.82	2.38	0.66
S2CLSc08.3	150.1065	2.2516	18.11	2.24	8.00	3.48	0.31	150.105 87	2.251 85	2.48	2.00	1.66
S2CLSc09	150.0568	2.3730	18.21	2.34	7.71	3.38	0.31	150.056 57	2.373 75	2.72	3.01	1.01
S2CLSc10	150.1504	2.3635	11.98	1.60	7.42	2.80	0.28	150.150 26	2.364 14	2.30	3.14	2.29
S2CLSc11	150.1874	2.3226	11.97	1.65	7.18	2.16	0.29	150.187 63	2.322 50	0.95	3.90	1.42
S2CLSc12	150.1541	2.3276	10.09	1.39	7.18	2.89	0.23	150.153 74	2.328 00	1.93	2.91	2.48
S2CLSc13	150.0780	2.2819	13.35	1.91	6.94	3.19	0.27	150.077 87	2.281 16	2.60	3.00	1.98
S2CLSc14	150.1390	2.4327	21.58	3.31	6.43	6.10	0.52	150.138 72	2.432 26	1.78	2.46	–
S2CLSc14.2	150.1390	2.4327	21.58	3.31	6.43	6.10	0.52	150.139 26	2.432 02	2.46	2.35	1.02
S2CLSc15	150.1096	2.2938	10.55	1.61	6.42	2.23	0.23	150.109 09	2.294 33	2.43	3.26	1.75
S2CLSc16	150.1235	2.3608	8.64	1.37	6.23	2.02	0.21	150.122 94	2.360 96	2.17	3.49	1.90
S2CLSc17	150.1040	2.3456	8.31	1.31	6.10	0.25	0.20	150.103 53	2.346 11	2.45	1.42	0.95
S2CLSc18	150.1219	2.3407	7.45	1.21	6.02	1.80	0.19	150.121 81	2.341 31	2.10	2.46	2.17
S2CLSc19	150.1837	2.3856	10.71	1.83	5.73	1.33	0.34	150.184 10	2.386 40	3.16	2.25	1.87

Table A1. *– continued*

ID	RA_{450} (°)	$Dec._{450}$ (°)	S_{450} (mJy)	ΔS_{450} (mJy)	SNR_{450}	S_{850} (mJy)	ΔS_{850} (mJy)	RA_{opt} (°)	$Dec._{opt}$ (°)	Sep. (arcsec)	$\log_{10}LR$	z_{phot}
S2CLSc20	150.0859	2.2971	9.88	1.82	5.44	1.07	0.26	150.085 79	2.297 65	2.12	3.28	0.98
S2CLSc21	150.1059	2.3256	7.13	1.29	5.42	1.22	0.20	150.105 31	2.325 90	2.35	2.39	0.84
S2CLSc22	150.0577	2.2929	11.58	2.09	5.38	2.86	0.28	150.057 06	2.292 86	2.39	3.06	1.33
S2CLSc23	150.0862	2.3807	11.38	2.15	5.11	1.82	0.31	150.085 99	2.380 83	0.93	2.46	0.31
S2CLSc23.2	150.0862	2.3807	11.38	2.15	5.11	1.82	0.31	150.086 33	2.380 91	0.97	2.28	1.46
S2CLSc23.3	150.0862	2.3807	11.38	2.15	5.11	1.82	0.31	150.086 26	2.381 42	2.67	1.39	2.34
S2CLSc24	150.0945	2.3350	7.29	1.41	5.08	0.44	0.21	*150.095 02*	*2.335 29*	*2.28*	*−1.64*	*0.05*
S2CLSc25	150.0815	2.3397	8.43	1.67	5.02	1.88	0.23	150.081 05	2.340 11	2.07	2.77	0.45
S2CLSc26	150.0855	2.2899	9.23	1.83	4.97	2.78	0.25	150.084 88	2.289 67	2.47	2.14	1.76
S2CLSc27	150.0769	2.3794	10.82	2.17	4.87	2.19	0.31	*150.077 20*	*2.380 38*	*3.71*	*0.54*	*2.56*
S2CLSc28	150.1223	2.3998	9.72	1.94	4.85	−0.19	0.29	150.122 26	2.399 77	0.25	3.16	0.47
S2CLSc28.2	150.1223	2.3998	9.72	1.94	4.85	−0.19	0.29	150.122 00	2.399 63	1.24	2.48	0.62
S2CLSc29	150.1594	2.2971	8.67	1.75	4.84	1.33	0.30	150.159 33	2.296 80	1.21	3.44	1.98
S2CLSc29.2	150.1594	2.2971	8.67	1.75	4.84	1.33	0.30	150.159 69	2.297 27	1.11	2.64	0.43
S2CLSc30	150.1571	2.3584	8.25	1.68	4.83	0.05	0.29	150.157 47	2.358 03	1.96	2.69	2.47
S2CLSc31	150.1177	2.3297	5.93	1.22	4.82	1.62	0.19	150.117 54	2.329 96	1.00	3.81	2.28
S2CLSc32	150.1011	2.3344	6.48	1.31	4.82	4.34	0.20	*150.101 19*	*2.334 37*	*0.48*	*−0.56*	–
S2CLSc33	150.0985	2.2601	9.73	2.00	4.77	3.94	0.28	150.097 90	2.260 01	2.20	1.75	–
S2CLSc34	150.1349	2.3991	8.90	1.81	4.76	2.24	0.29	150.135 13	2.399 42	1.52	3.11	0.07
S2CLSc35	150.1126	2.3750	8.21	1.68	4.75	2.98	0.25	150.112 40	2.375 25	1.29	2.97	2.21
S2CLSc36	150.0869	2.3082	8.33	1.75	4.73	−0.45	0.26	150.087 01	2.309 01	2.81	0.61	0.71
S2CLSc37	150.1180	2.2919	7.82	1.65	4.68	0.76	0.23	150.118 28	2.292 13	1.42	3.59	0.99
S2CLSc37.2	150.1180	2.2919	7.82	1.65	4.68	0.76	0.23	150.117 82	2.292 34	1.82	2.37	1.35
S2CLSc38	150.1308	2.3143	6.16	1.33	4.62	1.15	0.20	150.130 74	2.314 08	0.76	4.15	2.01
S2CLSc39	150.1464	2.3374	6.27	1.34	4.61	0.73	0.21	*150.147 22*	*2.337 19*	*2.89*	*−0.11*	*0.72*
S2CLSc40	150.1352	2.3702	7.01	1.52	4.51	1.06	0.24	150.136 11	2.370 52	3.37	1.78	0.81
S2CLSc41	150.1616	2.2684	9.97	2.17	4.49	0.99	0.33	*150.162 69*	*2.268 49*	*3.93*	*0.45*	*1.31*
S2CLSc42	150.1834	2.3899	8.56	1.88	4.45	0.90	0.35	150.183 68	2.390 47	2.23	3.59	1.80
S2CLSc43	150.1620	2.3408	6.84	1.56	4.36	1.03	0.26	150.161 86	2.340 92	0.64	1.20	0.66
S2CLSc44	150.1321	2.4024	8.29	1.89	4.33	1.63	0.29	150.131 88	2.403 20	2.87	3.04	3.03
S2CLSc45	150.0601	2.3022	9.19	2.11	4.33	0.05	0.27	*150.059 04*	*2.302 41*	*3.69*	*−0.11*	*0.81*
S2CLSc46	150.0672	2.3719	9.30	2.11	4.32	0.06	0.29	150.067 10	2.372 43	2.02	3.17	1.20
S2CLSc47	150.1770	2.3713	7.90	1.84	4.27	0.54	0.34	150.177 03	2.371 44	0.63	2.61	0.68
S2CLSc48	150.0846	2.2545	10.24	2.37	4.25	1.20	0.32	*150.085 24*	*2.255 21*	*3.43*	*0.94*	*1.01*
S2CLSc49	150.1296	2.2422	10.94	2.58	4.22	0.46	0.37	150.129 56	2.241 19	3.65	1.43	1.75
S2CLSc50	150.1434	2.4160	9.56	2.25	4.21	0.99	0.36	150.142 66	2.416 05	2.59	1.88	1.33
S2CLSc51	150.1874	2.3799	7.87	1.84	4.21	0.12	0.34	150.187 19	2.380 15	1.22	3.82	2.34
S2CLSc52	150.1677	2.2983	7.21	1.69	4.17	1.58	0.31	150.167 71	2.298 76	1.54	4.04	1.31
S2CLSc53	150.1660	2.3076	6.72	1.58	4.16	0.45	0.28	150.166 13	2.307 47	0.63	3.48	2.85
S2CLSc54	150.1941	2.3113	7.76	1.86	4.14	0.16	0.33	150.194 79	2.311 81	3.07	1.80	0.79
S2CLSc55	150.1299	2.2531	9.07	2.18	4.12	0.97	0.30	150.130 01	2.252 69	1.57	3.90	1.78
S2CLSc56	150.0683	2.2759	8.29	1.97	4.10	1.72	0.29	150.068 11	2.275 69	1.08	1.96	–
S2CLSc57	150.1521	2.3344	5.55	1.39	4.00	0.04	0.23	150.151 82	2.334 61	1.21	3.60	1.20
S2CLSc57.2	150.1521	2.3344	5.55	1.39	4.00	0.04	0.23	150.152 19	2.334 58	0.60	2.93	–
S2CLSc57.3	150.1521	2.3344	5.55	1.39	4.00	0.04	0.23	150.151 67	2.333 80	2.79	1.38	1.25
S2CLSc57.4	150.1521	2.3344	5.55	1.39	4.00	0.04	0.23	150.152 02	2.333 61	2.98	1.19	0.75

Table A2. 450-μm sources in the UDS CANDELS region. Sources with only unreliable identifications (i.e. $\log_{10}LR < 1.1$) are shown in italics. Where multiple good identifications for sources exist, these are listed with the suffix.2,.3, etc.

ID	RA_{450} (°)	$Dec._{450}$ (°)	S_{450} (mJy)	ΔS_{450} (mJy)	SNR_{450}	S_{850} (mJy)	ΔS_{850} (mJy)	RA_{opt} (°)	$Dec._{opt}$ (°)	Sep. (arcsec)	$\log_{10}LR$	z_{phot}
S2CLSu01	34.3639	−5.1991	21.63	2.83	7.51	5.46	0.38	34.3632	−5.199 37	2.80	3.20	2.22
S2CLSu01.2	34.3639	−5.1991	21.63	2.83	7.51	5.46	0.38	34.3645	−5.199 01	2.11	2.49	2.17
S2CLSu02	34.3341	−5.2182	27.60	4.16	6.47	5.34	0.51	34.3334	−5.218 25	2.43	3.37	2.15
S2CLSu03	34.3859	−5.1987	17.31	2.81	6.04	4.27	0.38	34.3857	−5.198 98	1.06	4.46	2.15
S2CLSu03.2	34.3859	−5.1987	17.31	2.81	6.04	4.27	0.38	34.3854	−5.198 69	1.82	2.11	2.15
S2CLSu03.3	34.3859	−5.1987	17.31	2.81	6.04	4.27	0.38	34.3863	−5.198 51	1.91	1.82	–
S2CLSu03.4	34.3859	−5.1987	17.31	2.81	6.04	4.27	0.38	34.3866	−5.198 87	2.80	1.66	2.12

Table A2 – *continued*

ID	RA_{450} (°)	$Dec._{450}$ (°)	S_{450} (mJy)	ΔS_{450} (mJy)	SNR_{450}	S_{850} (mJy)	ΔS_{850} (mJy)	RA_{opt} (°)	$Dec._{opt}$ (°)	Sep. (arcsec)	$\log_{10}LR$	z_{phot}
S2CLSu04	34.4077	−5.2630	27.36	4.71	5.79	3.00	0.64	*34.4068*	*−5.262 78*	*3.59*	*−0.03*	*2.58*
S2CLSu05	34.3721	−5.1977	15.86	2.80	5.51	1.95	0.37	34.3721	−5.197 91	0.89	3.74	2.58
S2CLSu06	34.3788	−5.1824	12.87	2.90	4.43	0.87	0.38	*34.3795*	*−5.182 32*	*2.78*	*−2.18*	*1.07*
S2CLSu07	34.3073	−5.1612	24.36	5.70	4.22	0.41	0.66	34.3067	−5.161 06	1.97	3.75	1.62
S2CLSu07.2	34.3073	−5.1612	24.36	5.70	4.22	0.41	0.66	34.3071	−5.161 46	1.30	3.15	1.40
S2CLSu07.3	34.3073	−5.1612	24.36	5.70	4.22	0.41	0.66	34.3074	−5.161 22	0.61	2.83	1.45
S2CLSu08	34.4326	−5.2390	18.73	4.40	4.14	0.65	0.69	34.4322	−5.239 56	2.37	2.01	–
S2CLSu09	34.3244	−5.2171	19.59	4.64	4.13	−0.43	0.53	*34.3248*	*−5.217 10*	*1.34*	*−0.86*	–
S2CLSu10	34.4601	−5.2013	21.62	5.24	4.11	2.88	0.80	34.4612	−5.201 34	3.92	1.95	2.07
S2CLSu11	34.3031	−5.2192	22.93	5.43	4.02	2.27	0.58	34.3022	−5.219 20	3.06	2.23	2.20
S2CLSu12	34.3384	−5.2532	17.83	4.37	4.01	2.89	0.55	34.3382	−5.254 08	3.26	1.62	0.82

Table A3. Multiwavelength photometry and derived quantities for the SCUBA-2 450-μm sources with robust counterparts and photometric redshifts.

ID	S_{250} (mJy)	ΔS_{250} (mJy)	S_{350} (mJy)	ΔS_{350} (mJy)	S_{450} (mJy)	ΔS_{450} (mJy)	S_{850} (mJy)	ΔS_{850} (mJy)	L_{IR} ($L_\odot$)	T_K (K)	β_D	M_* ($M_\odot$)	R_e (kpc)
c01	42.3	3.4	38.5	4.9	24.5	1.8	3.2	0.6	12.8 ± 0.2	$40.6^{+3.7}_{-3.2}$	$2.51^{+0.2}_{-0.2}$	11.3	0.47
c02	26.5	3.4	35.8	5.1	18.9	1.4	5.2	0.5	12.9 ± 0.3	$54.4^{+10.1}_{-6.9}$	$1.38^{+0.3}_{-0.3}$	10.5	0.47
c03	22.5	3.4	22.0	4.8	15.2	1.4	4.7	0.6	12.8 ± 0.2	$56.0^{+6.0}_{-6.5}$	$0.94^{+0.2}_{-0.2}$	10.2	0.28
c04	19.7	3.4	22.6	4.8	14.7	1.4	4.2	0.5	12.8 ± 0.3	$53.5^{+13.2}_{-8.6}$	$1.20^{+0.4}_{-0.4}$	10.7	0.04
c05	20.2	3.4	29.4	4.9	16.7	1.7	5.6	0.6	12.8 ± 0.1	$53.4^{+5.7}_{-5.5}$	$0.96^{+0.3}_{-0.2}$	10.8	0.45
c06	17.1	3.4	26.8	4.9	20.9	2.3	10.4	0.6	12.0 ± 0.1	$25.9^{+2.8}_{-3.7}$	$0.84^{+0.4}_{-0.2}$	11.2	0.50
c07	14.6	3.4	26.5	5.0	14.7	1.6	6.9	0.6	10.7 ± 0.2	$16.8^{+2.0}_{-2.6}$	$0.78^{+0.4}_{-0.2}$	10.7	0.17
c08	39.0	3.4	36.4	4.8	18.1	2.2	3.5	0.6	12.9 ± 0.2	$49.9^{+4.2}_{-4.2}$	$1.92^{+0.2}_{-0.2}$	10.2	0.55
c09	26.0	3.4	25.0	4.8	18.2	2.3	3.4	0.6	11.9 ± 0.3	$22.7^{+3.9}_{-2.8}$	$2.04^{+0.4}_{-0.4}$	10.6	−0.05
c10	11.1	3.4	17.0	4.9	12.0	1.6	2.8	0.6	12.4 ± 0.4	$36.1^{+10.4}_{-7.0}$	$1.95^{+0.6}_{-0.6}$	11.2	0.60
c11	19.0	3.4	15.8	5.2	12.0	1.6	2.2	0.6	12.0 ± 0.4	$34.0^{+21.8}_{-8.1}$	$1.74^{+0.6}_{-0.7}$	12.5	0.55
c12	12.7	3.4	15.0	4.9	10.1	1.4	2.9	0.5	12.6 ± 0.4	$51.0^{+14.9}_{-12.1}$	$1.22^{+0.6}_{-0.5}$	11.2	0.42
c13	9.8	3.4	25.6	6.2	13.4	1.9	3.2	0.6	12.2 ± 0.4	$28.4^{+6.9}_{-4.3}$	$2.20^{+0.5}_{-0.6}$	11.2	0.59
c15	13.0	3.4	13.4	4.9	10.6	1.6	2.2	0.6	12.2 ± 0.4	$36.3^{+18.2}_{-9.0}$	$1.64^{+0.7}_{-0.7}$	11.0	0.53
c16	10.3	3.4	15.0	4.9	8.6	1.4	2.0	0.5	12.1 ± 0.5	$39.3^{+20.8}_{-10.7}$	$1.52^{+0.7}_{-0.7}$	10.4	0.53
c17	17.5	3.4	13.3	4.9	8.3	1.3	0.2	0.5	11.9 ± 0.1	$46.4^{+2.2}_{-2.4}$	–	11.5	0.67
c18	10.3	3.4	7.5	4.8	7.5	1.2	1.8	0.5	12.3 ± 0.5	$50.6^{+24.1}_{-15.9}$	$1.21^{+0.8}_{-0.5}$	11.2	0.37
c19	18.2	3.4	14.7	4.9	10.7	1.8	1.3	0.6	12.5 ± 0.1	$53.5^{+5.7}_{-5.5}$	–	11.1	0.39
c20	26.6	3.4	16.2	5.0	9.9	1.8	1.1	0.6	12.1 ± 0.1	$37.5^{+1.3}_{-1.6}$	–	11.4	0.32
c21	5.3	3.4	5.8	4.9	7.1	1.3	1.2	0.5	11.4 ± 0.3	$40.5^{+14.6}_{-10.3}$	–	9.4	0.62
c22	10.1	3.4	2.7	5.1	11.6	2.1	2.9	0.6	11.7 ± 0.1	$27.2^{+2.7}_{-2.7}$	–	10.6	0.40
c23	10.2	3.4	6.7	4.8	11.4	2.1	1.8	0.6	10.5 ± 0.3	$32.3^{+8.7}_{-6.2}$	–	8.5	−0.06
c25	2.4	3.4	0.0	12.2	8.4	1.7	1.9	0.6	10.4 ± 0.2	$18.8^{+3.3}_{-3.1}$	–	9.4	0.50
c26	8.2	3.4	11.2	5.4	9.2	1.8	2.8	0.6	11.9 ± 0.1	$30.0^{+3.0}_{-3.3}$	–	10.7	0.25
c28	0.0	3.4	0.0	4.8	9.7	1.9	−0.2	0.6	11.6 ± 0.3	$42.0^{+35.1}_{-31.0}$	–	9.6	0.55
c29	6.6	3.4	12.2	5.1	8.7	1.7	1.3	0.6	12.1 ± 0.1	$40.3^{+5.2}_{-4.8}$	–	11.1	0.44
c30	11.3	3.4	14.0	4.9	8.3	1.7	0.0	0.6	12.0 ± 0.2	$78.1^{+15.2}_{-27.0}$	–	9.9	0.32
c31	4.4	3.4	9.8	5.1	5.9	1.2	1.6	0.5	12.1 ± 0.1	$36.2^{+4.9}_{-5.1}$	–	10.9	0.45
c34	6.8	3.4	4.9	4.8	8.9	1.8	2.2	0.6	8.8 ± 0.2	$18.0^{+3.6}_{-3.1}$	–	8.4	−0.93
c35	13.3	3.4	8.0	6.9	8.2	1.7	3.0	0.6	12.4 ± 0.4	$51.0^{+11.8}_{-12.0}$	$0.84^{+0.5}_{-0.3}$	11.1	0.47
c37	9.8	3.4	7.8	4.9	7.8	1.7	0.8	0.6	11.4 ± 0.2	$25.6^{+2.8}_{-2.8}$	–	11.8	0.52
c38	9.7	3.4	5.2	5.2	6.2	1.3	1.1	0.5	12.3 ± 0.2	$50.7^{+8.5}_{-8.4}$	–	10.8	0.34
c39	22.3	3.4	11.4	5.2	6.3	1.3	0.7	0.5	11.7 ± 0.1	$40.7^{+1.3}_{-1.5}$	–	10.9	0.32
c40	22.3	3.4	18.5	5.1	7.0	1.5	1.1	0.6	11.9 ± 0.1	$31.5^{+1.0}_{-1.0}$	–	12.0	0.35
c42	10.4	3.4	12.0	4.9	8.6	1.9	0.9	0.6	12.4 ± 0.2	$61.8^{+13.7}_{-10.8}$	–	10.7	0.61
c43	12.8	3.4	5.3	4.8	6.8	1.6	1.0	0.6	11.0 ± 0.1	$17.6^{+1.3}_{-1.4}$	–	12.8	0.82
c46	7.8	3.4	6.1	5.0	9.3	2.1	0.1	0.6	11.9 ± 0.4	$71.3^{+19.6}_{-29.7}$	–	11.2	0.32
c47	0.0	8.8	3.6	4.8	7.9	1.8	0.5	0.6	11.5 ± 0.3	$66.8^{+22.3}_{-29.9}$	–	9.2	0.60

Table A3. *– continued*

ID	S_{250} (mJy)	ΔS_{250} (mJy)	S_{350} (mJy)	ΔS_{350} (mJy)	S_{450} (mJy)	ΔS_{450} (mJy)	S_{850} (mJy)	ΔS_{850} (mJy)	$L_{\rm IR}$ ($L_\odot$)	$T_{\rm K}$ (K)	$\beta_{\rm D}$	M_* ($M_\odot$)	R_e (kpc)
c49	0.0	4.9	0.0	9.5	10.9	2.6	0.5	0.6	12.6 ± 0.5	$75.4^{+16.4}_{-25.1}$	–	11.4	0.54
c50	0.0	7.2	0.0	8.6	9.6	2.3	1.0	0.6	12.3 ± 0.5	$75.3^{+16.6}_{-24.8}$	–	10.0	0.21
c51	10.6	3.4	12.6	4.9	7.9	1.8	0.1	0.6	12.4 ± 0.2	$86.2^{+9.8}_{-18.1}$	–	11.9	0.32
c52	7.7	3.4	11.0	5.0	7.2	1.7	1.6	0.6	11.6 ± 0.2	$30.1^{+4.1}_{-3.8}$	–	10.6	0.42
c53	3.0	3.4	4.1	4.9	6.7	1.6	0.5	0.6	12.3 ± 0.3	$72.8^{+18.0}_{-23.4}$	–	10.5	0.03
c54	14.4	3.4	6.1	4.9	7.8	1.9	0.2	0.6	11.4 ± 0.1	$51.1^{+3.6}_{-4.2}$	–	10.8	0.57
c55	13.5	3.4	10.9	4.9	9.1	2.2	1.0	0.6	12.6 ± 0.3	$77.4^{+13.2}_{-16.1}$	–	10.4	0.29
c57	10.0	3.4	7.5	5.3	5.5	1.4	0.0	0.5	12.1 ± 0.5	$76.4^{+16.3}_{-25.5}$	–	12.0	0.53
u01	36.7	3.6	38.7	4.0	21.6	2.8	5.5	0.6	12.9 ± 0.3	$47.5^{+10.0}_{-6.6}$	$1.58^{+0.3}_{-0.4}$	11.4	0.62
u02	38.9	3.6	43.7	4.1	27.6	4.2	5.3	0.7	12.9 ± 0.3	$35.9^{+4.8}_{-3.3}$	$2.31^{+0.3}_{-0.3}$	11.4	0.64
u03	37.9	3.6	35.4	4.1	17.3	2.8	4.3	0.6	12.9 ± 0.5	$56.3^{+19.2}_{-10.5}$	$1.45^{+0.4}_{-0.4}$	11.0	0.59
u05	13.7	3.6	15.0	4.1	15.9	2.8	3.9	0.6	12.5 ± 0.4	$40.6^{+12.5}_{-8.3}$	$1.70^{+0.7}_{-0.7}$	10.5	0.16
u07	37.1	3.6	22.2	4.1	24.4	5.7	0.4	0.8	13.0 ± 0.5	$73.8^{+15.9}_{-11.2}$	$2.80^{+0.1}_{-0.2}$	11.4	0.33
u10	43.8	3.6	35.2	6.0	21.6	5.2	2.9	0.9	12.9 ± 0.5	$47.6^{+21.3}_{-8.5}$	$2.20^{+0.4}_{-0.6}$	11.0	0.49
u11	13.6	3.6	12.5	5.2	22.9	5.4	2.3	0.8	12.5 ± 0.4	$39.8^{+21.1}_{-8.9}$	$1.89^{+0.7}_{-0.9}$	11.2	0.38
u12	5.6	3.6	7.8	4.9	17.8	4.4	2.9	0.7	11.1 ± 0.2	$18.9^{+2.4}_{-2.5}$	–	10.4	0.14

Table B1. Limits on the parameters in the SED fitting.

Parameter	Min	Max
$\log_{10} L_{\rm IR}$ ($L_\odot$)	9	14
$T_{\rm D}$ (K)	5	100
$\beta_{\rm D}$	0.5	3.5
ν_0	100	100

APPENDIX B: MCMC FITTING TECHNIQUE

The modified blackbody parameters are inferred from the observed SEDs using an MCMC methodology. Specifically, the posterior probability density is mapped using a Metropolis–Hastings algorithm with Gibbs sampling. Parameters are constrained to take realistic values with a top-hat prior. The parameter constraints used in this work are given in Table B1.

The likelihood is estimated via use of the χ^2 statistic. 10 parallel MCMC chains are run, with convergence checks performed every 400 iterations, after an initial burn-in of 2000 iterations. Convergence is assessed using the method of Gelman & Rubin (1992). After convergence is achieved, a further 2000 iterations are performed, with inference performed on the last 2200 iterations from each chain.

APPENDIX C: STACKING FOR CONFUSION-LIMITED SUBMM IMAGING

As multiwavelength coverage of extragalactic survey fields has become common place, the practice of stacking images based on a selection at another, potentially deeper, wavelength has become popular. However, a major difficulty in this approach is the mismatched resolution between data sets, e.g. the optical and submm data sets used in this work have angular resolutions that are different by a factor of roughly 100. This means that the 'raw' stacked signal (i.e. just the pixels combined together) may not only contain a signal from the sources in the input list, but also those that are correlated spatially with them. It is important to note that the corruption of the stacking signal is solely due to these correlations; if galaxies were purely Poisson distributed, then simply measuring the covariance between the pixels coincident with sources would give an unbiased estimate of their mean flux density (e.g. Marsden et al. 2009).

Recently, a number of authors have presented methods to deal with these correlations. B12a use a traditional stacking method, but correct for the clustering signal via the use of simulations. Meanwhile Kurczynski & Gawiser (2010, hereafter KG10) offer an approach which uses linear algebra to account for the correlations between sources in the input list. Other methodologies exist but mainly fall into these two categories. Both of these methods have significant drawbacks. In principle, the B12a method can completely correct for the clustered signal, but it requires perfect knowledge of the clustering properties of the galaxies in the stacking list, something which is difficult to obtain given that we know clustering is a function of the intrinsic galaxy properties (e.g. SFR, stellar mass, morphology, etc.). The KG10 approach again offers the ability to completely correct the estimates, but this time requires the stacking input list to be complete; only correlations with galaxies in the input list can be taken into account. Thus, the two approaches suit different applications; if the source list to be stacked is incomplete but homogeneous, then the first approach is better, if it is quite complete but potentially heterogeneous, then the second approach should be used.

As an aside, a small number of papers have suggested that the best method to remove correlations is to fit for bright sources and then stack 'source-free' maps (e.g. Chary, Cooray & Sullivan 2008). However, this approach requires perfect knowledge of the source photometry, otherwise it is likely to introduce artefacts that can become significant if correlations between the bright sources and faint stacking list exist.

Given the depth of the CANDELS imaging available in the UDS and COSMOS fields, we make use of a KG10-like approach to stack the submm imaging, although with some mathematical tweaks.

To begin, we assume that the PRF is circularly symmetric and so can be described in one dimension as a function of the radial

distance from the source position. This assumption is for simplicity and to reduce the computational expense of the stacking calculation; all the following formalism can be easily expanded to consider the full 2D stacked image. For a 1D stack, the flux density for a single source x at a distance r is given by

$$s(r) = 1/N_r \sum d(x + r),$$

where d is the image, and the sum runs over the N_r pixels that lie at a separation r from the source position. It is clear that the simplest 1D stack for a list of source positions $\boldsymbol{x}$ is then

$$\bar{s(r)} = \frac{1}{N_r N_x} \sum_r \sum_x d(x + r).$$

If image pixels in d appear more than once in the summation, then this estimation for the stacked 1D source profile will be biased, giving erroneously high values of $\bar{s(r)}$ and broader source profiles. To correct this, we need to include information about the correlations between the pixels to be stacked. We can re-write the above equation in matrix notation as

$$\bar{\boldsymbol{s}} = \mathbf{A}\mathbf{d}, \tag{C1}$$

where $\mathbf{A}$ is an $N_d \times N_r$ matrix which contains the value $1/(N_x N_r)$ at the pixel coordinate that corresponds to a source x and separation r. For a source list without correlations, the columns of $\mathbf{A}$ would contain at most one non-zero value. This means that for an uncorrelated source list $\mathbf{A}^{\mathrm{T}}\mathbf{A} = \mathbf{I}$, where $\mathbf{I}$ is the identity matrix. If correlations between sources in the list exist, then $\mathbf{A}^{\mathrm{T}}\mathbf{A}$ will be a symmetric matrix that describes these correlations. Thus, it can be shown that an unbiased estimate of the mean 1D profile is given by

$$\mathbf{A}^{\mathrm{T}}\mathbf{A}\bar{\boldsymbol{s}} = \mathbf{A}\mathbf{d}. \tag{C2}$$

Letting $\mathbf{A}^{\mathrm{T}}\mathbf{A} = \mathbf{P}$ and $\mathbf{A}\mathbf{d} = \mathbf{b}$, this is now a linear equation of the form $\mathbf{b} = \mathbf{P}\mathbf{s}$, which can be solved efficiently via conjugate gradient methods (as the matrix $\mathbf{P}$ is non-negative and symmetric). In this formalism, $\mathbf{b}$ can be interpreted as the 'naive stack', i.e. the stack we would get by simply adding up the pixel flux from the map for each source, while $\mathbf{P}$ is the Fisher information matrix. Measurement errors in the image can be included naturally by re-writing $\mathbf{P}$ and $\mathbf{b}$ as

$$\mathbf{P} = \mathbf{A}^{\mathrm{T}}\mathbf{N}^{-1}\mathbf{A},$$

$$\mathbf{b} = \mathbf{A}^{\mathrm{T}}\mathbf{N}^{-1}\mathbf{d}.$$

For stacking to give interpretable results, the source lists that go into the stack must be reasonably homogeneous. This creates a tension with our desire to stack as complete a sample as possible to account for all the correlations that may be present. Fortunately, the stacking methodology can be expanded so that any number of independent source lists can be stacked simultaneously to account for the correlations both within lists and between them.

Assuming now we have a set of source positions to be stacked $\bar{\boldsymbol{s}^1}, \bar{\boldsymbol{s}^2}, \ldots, \bar{\boldsymbol{s}^N}$, we can create matrices $\mathbf{A}^1, \mathbf{A}^2, \ldots, \mathbf{A}^N$ that map the d into these N_t stacks. We can then re-write equation (C1) as

$$[\bar{\boldsymbol{s}}^1, \bar{\boldsymbol{s}}^2, ..., \bar{\boldsymbol{s}^N}] = \begin{matrix}[\mathbf{A}^1 \\ \mathbf{A}^2 \quad \mathbf{d} \\ \ldots \\ \mathbf{A}^N].\end{matrix}$$

Next we calculate $\mathbf{P}$ and $\mathbf{b}$ as before, although now $\mathbf{P}$ is an $N_r N_t \times N_r N_t$ matrix and the solution vector $\bar{\boldsymbol{s}}$ is of length $N_r N_t$ and contains the N_r 1D profiles for the N_t stacks.

SUPPORTING INFORMATION

Additional Supporting Information may be found in the online version of this article:

Table S1. Preliminary SCUBA-2 CLS 450 micron catalogue for COSMOS-DEEP region.

Table S2. Preliminary SCUBA-2 CLS 450 micron catalogue for UDS-DEEP region.

Table S3. SCUBA-2 + Herschel submm photometry for sources in Roseboom et al. 2013 (http://mnras.oxfordjournals.org/lookup/suppl/doi:10.1093/mnras/stt1577/-/DC1).

Please note: Oxford University Press are not responsible for the content or functionality of any supporting materials supplied by the authors. Any queries (other than missing material) should be directed to the corresponding author for the paper.

This paper has been typeset from a TEX/LATEX file prepared by the author.